

Combining Set Propagation with Finite Element Methods for Time Integration in Transient Solid Mechanics Problems

Marcelo Forets^a, Daniel Freire Caporale^b, Jorge M. Pérez Zerpa^c

^a*Departamento de Matemática y Aplicaciones, Centro Universitario Regional del Este, Universidad de la República, Maldonado, Uruguay*

^b*Instituto de Física, Facultad de Ciencias, Universidad de la República, Montevideo, Uruguay*

^c*Instituto de Estructuras y Transporte, Facultad de Ingeniería, Universidad de la República, Montevideo, Uruguay*

Abstract

The Finite Element Method (FEM) is the gold standard for spatial discretization in numerical simulations for a wide spectrum of real-world engineering problems. Prototypical areas of interest include linear heat transfer and linear structural dynamics problems modeled with linear partial differential equations (PDEs). While different algorithms for direct integration of the equations of motion exist, exploring all feasible behaviors for varying loads, initial states and fluxes in models with large numbers of degrees of freedom remains a challenging task. In this article we propose a novel approach, based in set propagation methods and motivated by recent advances in the field of Reachability Analysis. Assuming a set of initial states and input states, the proposed method consists in the construction of a union of sets (flowpipe) that enclose the infinite number of solutions of the spatially discretized PDE. We present the numerical results obtained in four examples to illustrate the capabilities of the approach, and draw some comparisons with respect to reference numerical integration methods. We conclude that the proposed method presents specific and promising advantages, but the full potential of reachability analysis in solid mechanics problems is yet to be explored.

Keywords: Reachability Analysis, Finite Element Method, Heat Transfer, Structural Dynamics, Numerical Verification

1. Introduction

Transient problems are of great relevance in a large and diverse set of disciplines in Engineering. For instance, Structural Dynamics problems with time-varying loads are formulated in notable key applications such as wind turbine modeling (Xue et al., 2020), wind energy production forecasting

(Prajapat et al., 2017), or the study of nonlinear behavior of cables (Martinelli & Perotti, 2001; Battini, 2018). Other transient problems are formulated and solved using heat transfer analysis, for diverse applications ranging from designing massive concrete structures (Wilson et al., 1974; Tahersima & Tikalsky, 2017) to simulating the effects of breathing disorders, such as COVID-19, on the respiratory tract (Grau-Bartual & Al-Jumaily, 2020).

The mathematical models developed and applied to any real-world problem are all subject to one inherent feature: *parameter uncertainty*. The material properties, the loads applied, the geometries, etc., must be provided as an input of the models, and are always submitted to errors. Hence, the effect of parameter uncertainty over simulation results must be quantified. In the last decades, several methods have been developed using different mathematical and numerical techniques, which can be classified into probabilistic and non-probabilistic approaches. The main probabilistic approaches are Uncertainty Propagation and Monte Carlo methods. The former is based on the calculation of probability density functions for sampling statistics and has been successfully applied in structural systems under dynamic loads (Capillon et al., 2016; Imholz et al., 2020; Hornshøj-Møller et al., 2021). Monte Carlo methods rely on repeated numerical simulations starting from different initial conditions and parameter choices (Shinozuka, 1972). Non-probabilistic approaches include interval methods (Shu-Xiang & Zhen-zhou, 2001; Muhanna & Mullen, 2011), and fuzzy logic methods (Muhanna & Mullen, 1999).

The governing equations of the mathematical models arising in heat transfer and structural mechanics problems are commonly expressed in terms of Partial Differential Equations (PDEs). PDEs are numerically solved considering both a discretization in space and time. The Finite Element Method (FEM) emerged in the second half of the 20th century (Zienkiewicz, 1972) and, after the development of several numerical techniques (Bathe, 1982) and theoretical error bounds (Ladeveze & Leguillon, 1983; Hughes, 1987), it has become the gold-standard approach for spatial discretization of PDEs. The first applications of the FEM were mainly in structural and mechanical engineering problems, see e.g. (Oñate, 2009). Nowadays, a diverse and vast set of different applications surged, ranging from accurately modeling arterial blood flows (Urquiza et al., 2006) to studying habits of prehistoric mammals (Patiño et al., 2019).

Regarding the resolution of transient problems, numerical time integration methods are being actively developed (Bathe & Noh, 2012; Kim & Choi, 2018; Malakiyeh et al., 2019; Li et al.,

2017), highlighting the challenge this represents. Moreover, a large set of numerical tools have been developed, including open source software for FEM analysis (Maas et al., 2012; Hecht, 2012), efficient mesh discretization (Geuzaine & Remacle, 2009) and visualization of numerical results (Ahrens et al., 2005).

The most common practice to solve transient problems relies on exploring different behaviors by simulation and testing. However, if uncertainty is present and the application requires an exhaustive exploration of the state space, such approach becomes computationally intractable. For instance, to guarantee that a certain maximum temperature in a massive concrete structure is not exceeded (Tahersima & Tikalsky, 2017) can be interpreted as a *verification problem*. A prominent framework used to solve verification problems consists in approximating the set of states that are reachable by a dynamical system, from all initial states and for all admissible inputs and parameters. Such approach is called *reachability analysis* and it has been recently applied to solve verification, control, path planning and stability problems in diverse domains (e.g. aerospace, analog/mixed signal circuits, automotive, power systems, robotics and systems biology) (Althoff et al., 2020b). One of the main approaches to reachability analysis relies on *set propagation*, where the solution of an ordinary differential equation (ODE) is expressed in terms of sets rather than numbers. Several algorithms have been devised for linear (Girard et al., 2006b; Le Guernic & Girard, 2010; Althoff & Frehse, 2016; Bogomolov et al., 2018) and non-linear (Henzinger et al., 1998; Asarin et al., 2003; Althoff et al., 2008; Chen et al., 2013) differential equations, as well as for hybrid systems, i.e. mixing discrete and continuous dynamics (Frehse et al., 2011; Benvenuti et al., 2008). Despite the existence of numerous algorithms, their successful application requires expert knowledge about algorithm tuning (Wetzlinger et al., 2020). The main motivation of our work is to integrate reachability analysis and finite element methods in structural analysis applications.

In this article we present a new framework for the resolution of linear transient dynamics problems in solid mechanics that builds upon set propagation techniques. Starting from the assembled FEM system of differential equations, our method is based on three stages: homogeneization, conservative time discretization, and set propagation. Homogeneization consists of reformulating the governing equations as an homogeneous first order system with set-valued initial conditions and external inputs. The time discretization strategy that we have applied represents an improvement over previously used algorithms. Finally, we evaluated several set propagation strategies

and for each problem considered we report the most convenient one. In order to implement the methodology proposed in the present article, we developed an open source toolkit that is based on JuliaReach¹, a state-of-the-art open source library for reachability analysis, and ONSAS², a finite-element structural analysis solver.

The approach in the present article is similar in spirit to (Scacchioli et al., 2014). The authors use ellipsoidal set representations; however, for systems with many degrees of freedom, such approach does not scale well. In (Bak et al., 2019) the authors develop a set propagation method based on linear programming that is applied to a heat diffusion problem with a large (1000^3) mesh obtained using finite differences. In comparison with our technique, theirs' is more scalable, at the expense of returning reach-set approximations at time points, instead of reach-sets at time intervals as in our method. In (Althoff, 2019) the author extended the theoretical basis of set propagation to handle large linear systems with Krylov subspace approximations of the state transition matrix acting on zonotopes. Their results are illustrated on the finite element model of a bridge subject to set-valued wind forces. Introducing Krylov subspace approximations to enhance the scalability of our methodology is an interesting avenue for future research.

A typical assumption in reachability computations is to consider bounded but arbitrarily varying inputs. While that input model is very general, it may be too pessimistic (conservative) and it can lead to unsatisfactorily coarse results. We demonstrate that when a family of admissible behaviors for the input functions is given, such issue is substantially mitigated by homogeneization of the governing equations under set-valued initial conditions and inputs, thereby reducing the overapproximation error.

It is important to recall that the solution of the FEM equations, or spatially discrete system of ODEs, is already in error when compared with the original exact problem in the continuum. Estimating and absorbing such error in a set-based fashion is not addressed in this article. Moreover, it is well-known that high order modes are artifacts of the discretization process, thus numerical or algorithmic dissipation is often a favorable or even required mechanism to improve the accuracy of the results when compared to the exact problem (Hughes, 1987). We think that flowpipe solutions, while not being numerically damped, may provide a practical insight into the degree to which the numerical solutions depart from the true trajectories of the FEM equations.

¹<http://juliareach.com>

²<http://www.onsas.org>

This article is organized as follows. In Section 2 the basic concepts of the Finite Element Method and Reachability Analysis are described, including an illustrative example complementing the presentation of the latter. In Section 3 the key components of the proposed methodology are developed. In Section 4 the results obtained considering four numerical examples (including reference examples from the literature and a realistic Engineering problem) are shown. Finally, in Section 5 the conclusions are exposed and additional proofs are available as part of the Appendix.

2. Preliminaries

In this section a brief description of basic preliminary notions is presented. The content of this section is well-documented in the literature. It is included in order to provide a self-contained presentation of the methodology.

We begin describing the systems of differential equations obtained by using the Finite Element Method for the two types of solid mechanics problems considered in this work: heat transfer and structural dynamics problems. After that, a description of three of the reference numerical time-integration methods is presented. Finally, we recall some notions from reachability analysis including reach-sets, flowpipes and common set representations.

2.1. Transient problems governing equations

2.1.1. Heat transfer equations

In this section the equations of the heat transfer problem are presented. Let us consider a solid occupying a region Ω , with outward normal \mathbf{n} subject to: input heat fluxes q_{inp} on the boundary Γ_N (Neumann boundary conditions), temperature values $\tilde{\theta}$ on Γ_D (Dirichlet boundary conditions) and heat exchange on Γ_R (Robin boundary conditions), as it is shown in Figure 1. A volumetric internal heat source $Q_{int}(t)$ can also be present. Without loss of generality, the thermal conductivity of the solid is assumed isotropic, defined by a scalar field κ , and the density and specific heat are given by the scalar fields ρ and c , respectively.

The boundary conditions of the problem can be written as:

$$\begin{cases} \theta(\mathbf{x}, t) = \tilde{\theta}(\mathbf{x}, t) & \text{on } \Gamma_D \\ \kappa \frac{\partial \theta}{\partial \mathbf{n}}(\mathbf{x}, t) = q_{inp}(\mathbf{x}, t) & \text{on } \Gamma_N \\ -\kappa \frac{\partial \theta}{\partial \mathbf{n}}(\mathbf{x}, t) = h(\theta(\mathbf{x}, t) - \theta_\infty(t)) & \text{on } \Gamma_R \end{cases} \quad (1)$$

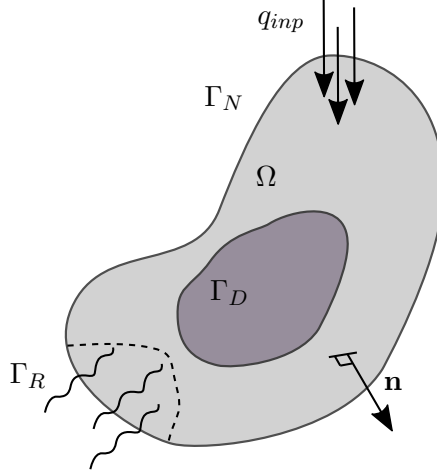


Figure 1: Diagram of a solid interacting with an environment through Dirichlet, Neumann and Robin boundary conditions.

where $\theta(\mathbf{x}, t)$ is the unknown temperature scalar field at position \mathbf{x} and time t , h is the convection coefficient and $\theta_\infty(t)$ is the ambient temperature at time t . Dirichlet boundary conditions are assumed homogeneous, thus we consider $\tilde{\theta}(\mathbf{x}, t) = 0$; the non-homogeneous case can be easily derived.

The heat transfer governing equations for a given time t can be defined by the *Principle of Virtual Thermal-Work* (Romano et al., 2010; Bathe, 2014). The variational identity, for any field of virtual temperatures $\delta\theta$, can be written as follows:

$$\int_{\Omega} \kappa \nabla \theta(t) \cdot \nabla \delta\theta \, dV + \int_{\Omega} \rho c \frac{\partial \theta}{\partial t}(t) \delta\theta \, dV = \int_{\Omega} Q_{int}(t) \delta\theta \, dV + \int_{\partial\Omega} \kappa \nabla \theta(t) \cdot \mathbf{n} \delta\theta \, dS \quad \forall \delta\theta \in \tilde{\mathcal{T}}, \quad (2)$$

where $\tilde{\mathcal{T}}$ is the set of virtual temperatures and the point \mathbf{x} is omitted for simplicity of notation. Substituting the boundary conditions given by Eq. (1) into Eq. (2) the following identity is obtained:

$$\begin{aligned} \int_{\Omega} \kappa \nabla \theta(t) \cdot \nabla \delta\theta \, dV + \int_{\Omega} \rho c \frac{\partial \theta}{\partial t}(t) \delta\theta \, dV + \int_{\Gamma_R} h \theta(t) \delta\theta \, dS &= \dots \\ \int_{\Omega} Q_{int}(t) \delta\theta \, dV + \int_{\Gamma_N} q_{inp}(t) \delta\theta \, dS + \int_{\Gamma_R} h \theta_\infty(t) \delta\theta \, dS &\quad \forall \delta\theta \in \tilde{\mathcal{T}}. \end{aligned} \quad (3)$$

The discretization of the spatial domain is done using the Finite Element Method (Wilson et al., 1974; Hughes, 1987). Interpolation functions are considered for the temperature and virtual temperature fields, obtaining the following expressions for the temperature within each element e : $\theta(\mathbf{x}, t) = \mathbf{N}^e(x) \boldsymbol{\theta}^e(t)$ and $\nabla \theta(\mathbf{x}, t) = \mathbf{B}^e(x) \boldsymbol{\theta}^e(t)$ for the gradients, where \mathbf{N}^e is the matrix of interpolation functions, \mathbf{B}^e is the matrix of derivatives and $\boldsymbol{\theta}^e(t)$ is the vector with the values

of temperatures at time t at the nodes of element e . Substituting these expressions for both temperature and virtual temperature fields, the spatial-discretized equations are obtained:

$$\mathbf{C}_\theta \dot{\boldsymbol{\theta}}(t) + \mathbf{K}_\theta \boldsymbol{\theta}(t) = \mathbf{f}_\theta(t), \quad (4)$$

where the matrix \mathbf{K}_θ is the assembled convection matrix

$$\mathbf{K}_\theta = \bigoplus_{e=1}^{n_e} \mathbf{K}_\theta^e, \quad \mathbf{K}_\theta^e = \int_{\Omega^e} \kappa (\mathbf{B}^e)^T \mathbf{B}^e dV + \int_{\Gamma_R^e} h (\mathbf{N}^e)^T \mathbf{N}^e dS, \quad (5)$$

with n_e being the number of elements, the matrix \mathbf{C}_θ is the assembled diffusion matrix

$$\mathbf{C}_\theta = \bigoplus_{e=1}^{n_e} \mathbf{C}_\theta^e \quad \mathbf{C}_\theta^e = \int_{\Omega^e} \rho c (\mathbf{N}^e)^T \mathbf{N}^e dV, \quad (6)$$

and the vector $\mathbf{f}_\theta(t)$ is given by

$$\mathbf{f}_\theta(t) = \bigoplus_{e=1}^{n_e} \int_{\Omega^e} Q_{int}(t) \mathbf{N}^e dV + \int_{\Gamma_N^e} q_{inp}(t) \mathbf{N}^e dS + \int_{\Gamma_R^e} h \theta_\infty(t) \mathbf{N}^e dS. \quad (7)$$

The initial conditions of the problem are given by $\theta(\mathbf{x}, 0) = \theta_0(\mathbf{x})$, where θ_0 is the initial temperature field.

It is important to highlight that the diffusion matrix \mathbf{C}_θ is a square positive definite matrix, therefore, it is invertible.

2.1.2. Structural dynamics equations

Let us consider a solid body occupying a region Ω with boundary Γ_S with outward normal \mathbf{n} , as it is shown in Figure 2. The boundary is a disjoint union of boundaries $\Gamma_{\mathbf{t},S}$ and $\Gamma_{\mathbf{u},S}$, i.e. $\Gamma_S = \Gamma_{\mathbf{u},S} \cup \Gamma_{\mathbf{t},S}$ and $\Gamma_{\mathbf{u},S} \cap \Gamma_{\mathbf{t},S} = \emptyset$. Loads per unit area $\bar{\mathbf{f}}(t)$ and displacements $\bar{\mathbf{u}}(t)$ are prescribed at Γ_N and Γ_D , respectively. For the sake of simplicity and without loss of generality, homogeneous displacement boundary conditions are considered (i.e., $\bar{\mathbf{u}}(t) = 0$).

The solid is assumed to be formed by a linear elastic material with Young modulus E , Poisson ratio ν (both associated with a constitutive tensor \mathbb{C}), and mass density ρ . The governing equations for the local displacement field $\mathbf{u}(\mathbf{x}, t)$ can be obtained using the Principle of Virtual Work and the Finite Element Method (Bathe, 2014; Hughes, 1987), resulting in:

$$\mathbf{M}_\mathbf{u} \ddot{\mathbf{u}}(t) + \mathbf{C}_\mathbf{u} \dot{\mathbf{u}}(t) + \mathbf{K}_\mathbf{u} \mathbf{u}(t) = \mathbf{f}_\mathbf{u}(t), \quad (8)$$

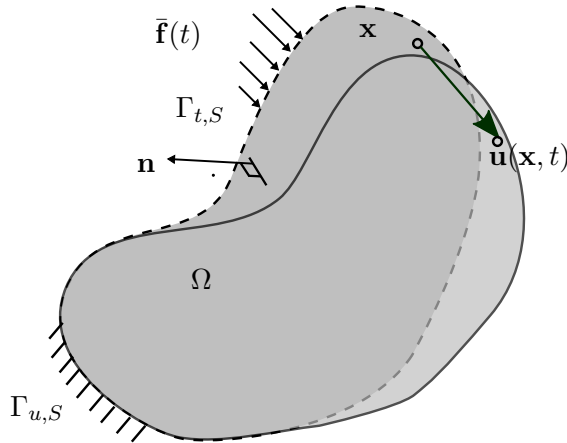


Figure 2: Diagram of a solid interacting with an environment through an external load distributed over its boundary.

where \mathbf{K}_u is the stiffness matrix, given by:

$$\mathbf{K}_u = \bigwedge_{e=1}^{n_e} \mathbf{K}_u^e, \quad \mathbf{K}_u^e = \int_{\Omega^e} (\mathbf{B}_u^e)^T \mathbb{C} \mathbf{B}_u^e dV, \quad (9)$$

and \mathbf{M}_u is the mass matrix, given by:

$$\mathbf{M}_{\mathbf{u}} = \bigwedge_{e=1}^{n_e} \mathbf{M}_{\mathbf{u}}^e, \quad \mathbf{M}_{\mathbf{u}}^e = \int_{O^e} \rho (\mathbf{N}_u^e)^T \mathbf{N}_u^e \, dV, \quad (10)$$

where the matrices \mathbf{N}_u^e and \mathbf{B}_u^e are the matrices given by the interpolation functions and gradients for the displacement fields. The viscosity (or damping) matrix \mathbf{C}_u is assumed to be known or estimated as a combination of the stiffness and the mass matrices (Clough & Penzien, 1993).

It is important to highlight that the assembled mass matrix $\mathbf{M}_{\mathbf{u}}$ is a square positive definite matrix, therefore, it is invertible.

2.2. Numerical Integration Methods

In this section, a minimal description of the reference numerical time-integration methods is presented. In all the methods described, a fixed time step Δt is considered, and the time domain is discretized in values $t_k = \Delta t \cdot k$ with k being a natural number. Each time t_k might also be referred to as k .

2.2.1. Backward Euler method for heat transfer

The space-discretized equations of the heat transfer problem presented in Eq. (4) can be approximately solved by considering the identity at time k :

$$\mathbf{K}_\theta \boldsymbol{\theta}(t_k) + \mathbf{C}_\theta \dot{\boldsymbol{\theta}}(t_k) = \mathbf{f}_\theta(t_k), \quad (11)$$

with the initial conditions given by a known field of temperatures $\boldsymbol{\theta}(t^{(0)}) = \boldsymbol{\theta}_0$.

One of the reference methods for numerical integration of heat transfer problems is the Backward Euler method. In this method the first time-derivative of the temperature field is approximated using the following backward difference approximation:

$$\dot{\boldsymbol{\theta}}_{k+1} = (\boldsymbol{\theta}_{k+1} - \boldsymbol{\theta}_k)/\Delta t, \quad (12)$$

where the compact notation $\boldsymbol{\theta}_k = \boldsymbol{\theta}(t_k)$ is adopted. Substituting Eq. (12) into Eq. (11) and considering time t_{k+1} we obtain:

$$(\mathbf{K}_\theta \Delta t + \mathbf{C}_\theta) \boldsymbol{\theta}_{k+1} = \mathbf{f}_{\theta,k+1} \Delta t + \mathbf{C}_\theta \boldsymbol{\theta}_k, \quad (13)$$

which represents a well-posed linear system of equations that provides the temperature field at time $k + 1$.

2.2.2. The Newmark method for structural dynamics

The structural dynamics governing equations presented in Eq. (8) can also be numerically solved considering the identity at time k :

$$\mathbf{M}_u \ddot{\mathbf{u}}_k + \mathbf{C}_u \dot{\mathbf{u}}_k + \mathbf{K}_u \mathbf{u}_k = \mathbf{f}_{u,k}, \quad (14)$$

and a suitable numerical approach for the time integration.

One of the standard integration rules is the Newmark method, in which the displacements and velocities at time $k + 1$ are estimated using the following expressions:

$$\dot{\mathbf{u}}_{k+1} = \dot{\mathbf{u}}_k + [(1 - \beta)\ddot{\mathbf{u}}_k + \beta\ddot{\mathbf{u}}_{k+1}] \Delta t \quad (15)$$

$$\mathbf{u}_{k+1} = \mathbf{u}_k + \dot{\mathbf{u}}_k \Delta t + [(1/2 - \alpha)\ddot{\mathbf{u}}_k + \alpha\ddot{\mathbf{u}}_{k+1}] \Delta t^2, \quad (16)$$

where β and α are scalar parameters given by $\beta = 1/2$ and $\alpha = 1/4$ (Bathe, 2014). Substituting these approximations in Eq. (14) evaluated at time $k + 1$, the following linear system of equations is obtained:

$$(b_0 \mathbf{M}_u + b_1 \mathbf{C}_u + \mathbf{K}_u) \mathbf{u}_{k+1} = \mathbf{f}_{u,k+1} + \mathbf{M}_u (b_0 \mathbf{u}_k + b_2 \dot{\mathbf{u}}_k + \ddot{\mathbf{u}}_k) + \mathbf{C}_u (b_1 \mathbf{u}_k + \dot{\mathbf{u}}_k), \quad (17)$$

where the auxiliary constants $b_0 = 4/\Delta t^2$, $b_1 = 2/\Delta t$ and $b_2 = 4/\Delta t$ are introduced.

2.2.3. The Bathe method for structural dynamics

In the Bathe method (Bathe, 2014) an additional intermediate sub-step is introduced, thus for each time step two sub-steps are performed. First a Newmark approximation is used with a $\Delta t/2$ step size:

$$\dot{\mathbf{u}}_{(k+1/2)} = \dot{\mathbf{u}}_k + \frac{\Delta t}{4} (\ddot{\mathbf{u}}_k + \ddot{\mathbf{u}}_{(k+1/2)}) \quad (18)$$

$$\mathbf{u}_{(k+1/2)} = \mathbf{u}_k + \frac{\Delta t}{4} (\dot{\mathbf{u}}_k + \dot{\mathbf{u}}_{(k+1/2)}), \quad (19)$$

with the sub-index $(k+1/2)$ referring to the solutions at the mid-time step $\Delta t/2$. For the following sub-step a 3-point Backward Euler approximation is considered:

$$\dot{\mathbf{u}}_{k+1} = \frac{1}{\Delta t} \mathbf{u}_k + -\frac{4}{\Delta t} \mathbf{u}_{(k+1/2)} + \frac{3}{\Delta t} \mathbf{u}_{k+1} \quad (20)$$

$$\ddot{\mathbf{u}}_{k+1} = \frac{1}{\Delta t} \dot{\mathbf{u}}_k + -\frac{4}{\Delta t} \dot{\mathbf{u}}_{(k+1/2)} + \frac{3}{\Delta t} \dot{\mathbf{u}}_{k+1}. \quad (21)$$

After substituting the interpolations in the corresponding time dynamics equation the following systems of equations are obtained, to compute the solutions at the first sub-step:

$$(a_0 \mathbf{M}_{\mathbf{u}} + a_1 \mathbf{C}_{\mathbf{u}} + \mathbf{K}_{\mathbf{u}}) \mathbf{u}_{(k+1/2)} = \mathbf{f}_{\mathbf{u},(k+1/2)} + \mathbf{M}_{\mathbf{u}}(a_0 \mathbf{u}_k + a_4 \dot{\mathbf{u}}_k + \ddot{\mathbf{u}}_k) + \mathbf{C}_{\mathbf{u}}(a_1 \mathbf{u}_k + \dot{\mathbf{u}}_k), \quad (22)$$

and for the second sub-step:

$$\begin{aligned} (a_2 \mathbf{M}_{\mathbf{u}} + a_3 \mathbf{C}_{\mathbf{u}} + \mathbf{K}_{\mathbf{u}}) \mathbf{u}_{k+1} &= \mathbf{f}_{\mathbf{u},k+1} + \mathbf{M}_{\mathbf{u}}(a_5 \mathbf{u}_{(k+1/2)} + a_6 \mathbf{u}_k + a_1 \dot{\mathbf{u}}_{(k+1/2)} + a_7 \dot{\mathbf{u}}_k) \\ &+ \mathbf{C}_{\mathbf{u}}(a_1 \mathbf{u}_{(k+1/2)} + a_7 \mathbf{u}_k), \end{aligned} \quad (23)$$

where the auxiliary constants $a_0 = 16/\Delta t^2$, $a_1 = 4/\Delta t$, $a_2 = 9/\Delta t^2$, $a_3 = 3/\Delta t$, $a_4 = 8/\Delta t$, $a_5 = 12/\Delta t^2$, $a_6 = -3/\Delta t^2$ and $a_7 = -1/\Delta t$ were introduced.

2.3. Set propagation concepts

In this section we consider set-based integration in the context of linear differential equations and introduce two essential concepts: reach-set and flowpipe. Then we define the representations used in our approach: hyperrectangles, zonotopes and support functions. The definitions are illustrated by means of a textbook example: the harmonic oscillator. More complex and larger problems are considered in Section 4.

2.3.1. Illustrative example: harmonic oscillator

The set propagation definitions introduced in this section are illustrated using a single degree of freedom second order problem given by the following equation:

$$\ddot{u}(t) + \omega^2 u(t) = 0, \quad (24)$$

where ω is a scalar and u is the unknown. This problem can be associated with a spring-mass system, where $u(t)$ is the elongation of the spring at time t and the mass and stiffness set a natural frequency ω . In this case we consider $\omega = 4\pi$.

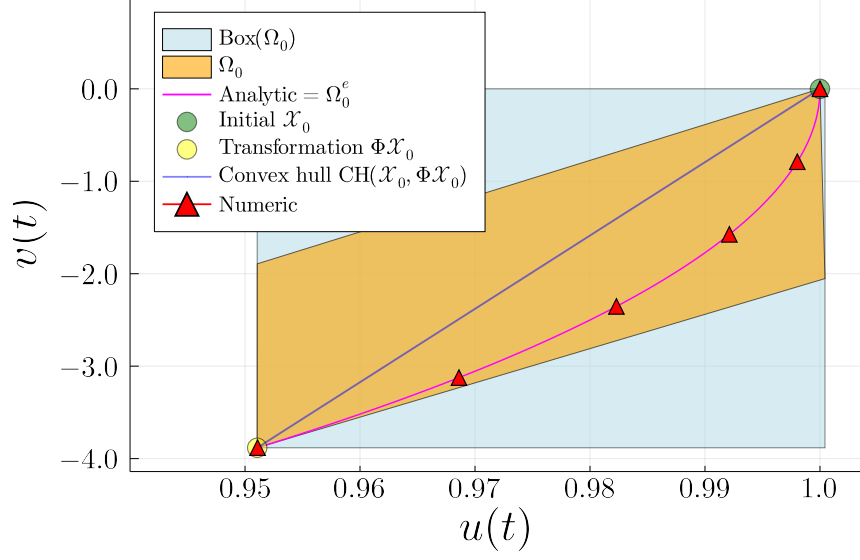
Let us introduce the state variable $v(t) := \dot{u}(t)$ and define the vector $\mathbf{x}(t) = [u(t), v(t)]^T$. Then Eq. (24) can be written in the following first order form

$$\dot{\mathbf{x}}(t) = \begin{bmatrix} 0 & 1 \\ -\omega^2 & 0 \end{bmatrix} \mathbf{x}(t). \quad (25)$$

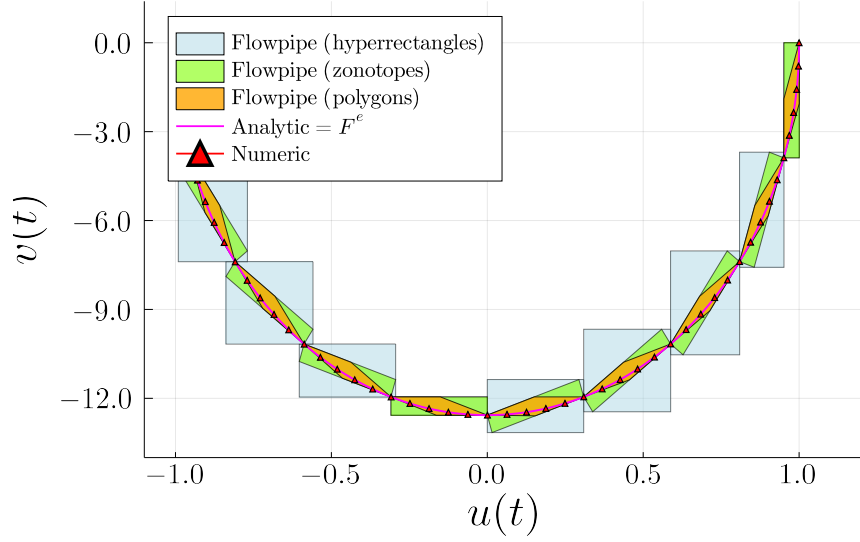
Two cases are considered for the initial conditions, first a single initial condition given by $u(0) = 1$ and $v(0) = 0$, and a second case where the initial conditions belong to a set. This problem is solved using set propagation and the results obtained for the single initial condition are shown in Fig. 3. The time step-size used is $\delta = 0.025$. The set Ω_0 from Fig. 3a includes the analytic trajectory within $[0, \delta]$, and such set is propagated to cover the solution for further time intervals as in Fig. 3b. It is worth noting that even when the initial condition is a singleton, the set propagation technique returns a sequence of sets, and such sequence guarantees an enclosure of the analytic solution at *any* time $t \in [0, T] \subset \mathbb{R}$. For comparison, we also plot the analytic solution of Eq. (25) (magenta solid line) and a numerical solution obtained using the Newmark's method with time step $\delta/5$ (red triangle markers). The figure shows other set representations and concepts that will be developed in the following paragraphs.

The result obtained when a set of initial conditions is considered is shown in Fig. 4, together with few dozen trajectories with random initial conditions drawn from the initial set $\mathcal{X}_0 = \mathcal{U}_0 \times \mathcal{V}_0 = [0.9, 1.1] \times [-0.1, 0.1]$, where \times denotes the Cartesian product.

In both cases, it is shown that a single set-based integration covers infinitely many trajectories *in dense time*, i.e. for all intermediate times between 0 and T , where $T > 0$ is the time horizon, there is a reach-set that covers all the exact solutions.

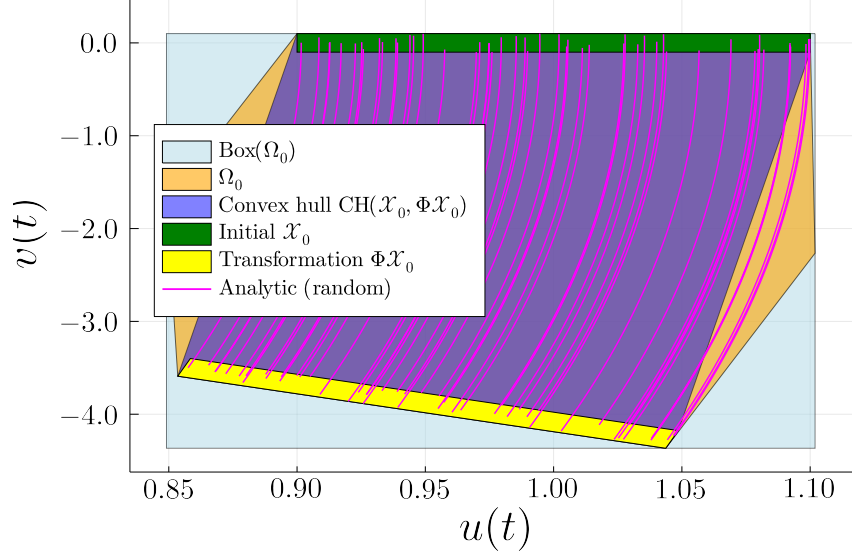


(a) The set Ω_0 (orange) encloses the true solution (magenta) at the endpoints and at any intermediate time between 0 and $\delta = 0.025$.

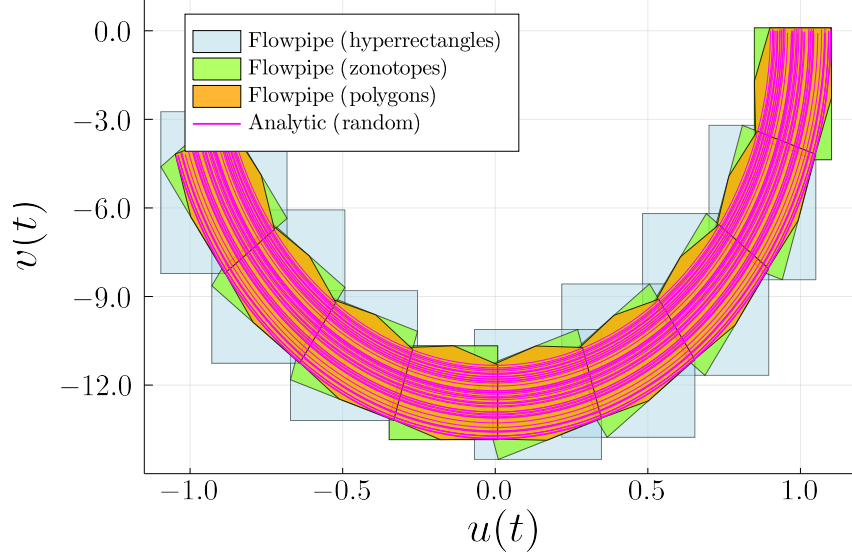


(b) Set propagation using hyperrectangles (lightblue), zonotopes (green) and to assess the zonotopic overapproximation of Ω_0 , polygons (orange).

Figure 3: Illustration of set-based integration of the simple harmonic oscillator example with single initial condition. Shown are phase-space plots $u(t)$ vs. $v(t)$ for the first reach-set (Fig. 3a), and for the first 9 reach-sets (Fig. 3b).



(a) The set Ω_0 (orange) covers the right-most trajectories for intermediate times, which naturally escape linear interpolations (violet).



(b) The flowpipe construction method for Eq. (35) is wrapping-free: the area of the sets does not increase with time.

Figure 4: Illustration of set-based integration of the simple harmonic oscillator with distributed initial conditions. Note that a single set-based integration covers all dynamically feasible behaviors: to illustrate this fact we plot 50 analytic solutions (magenta) uniformly distributed over \mathcal{X}_0 .

2.3.2. Trajectories, reach-sets and flowpipes

Let us consider an initial-value problem

$$\dot{\mathbf{x}}(t) = \mathbf{A}\mathbf{x}(t), \quad \mathbf{x}(0) \in \mathcal{X}_0, \quad t \in [0, T], \quad (26)$$

with state matrix $\mathbf{A} \in \mathbb{R}^{n \times n}$ and where $\mathbf{x}(t) \in \mathbb{R}^n$ is the state vector at time t . The initial condition is $\mathbf{x}(0) \in \mathcal{X}_0 \subset \mathbb{R}^n$ with \mathcal{X}_0 a closed and convex set. In this article we will refer to any state belonging to \mathcal{X}_0 as an *admissible* state. The guiding principle in set-based integration is to represent reachable states using sets in the Euclidean space that are *propagated* according to the system's dynamics. The obtained sequence of sets, by construction, covers the exact trajectories for given time intervals, for any admissible initial condition or external actions. For instance, the result for the harmonic oscillator presented in Section 2.3.1 using a single initial condition is shown in Fig. 3 (green circle), and in Fig. 4 (green box) the results for a box of initial conditions are shown.

Given the system of ODEs in Eq. (26), a *trajectory* from an initial state \mathbf{x}_0 is the solution for a given initial condition $\mathbf{x}(0) = \mathbf{x}_0$, denoted $\varphi(\mathbf{x}_0, t) : \mathbb{R}^n \times [0, T] \rightarrow \mathbb{R}^n$, which we know is $\varphi(\mathbf{x}_0, t) = e^{\mathbf{A}t}\mathbf{x}_0$. The *reach-set* at a *time point* $t \in [0, T]$ is

$$\mathcal{R}^e(\mathcal{X}_0, t) := \{\varphi(\mathbf{x}_0, t) : \mathbf{x}_0 \in \mathcal{X}_0\}. \quad (27)$$

This is the set of states which are reachable at time t starting from any admissible initial condition. Generalizing Eq. (27) to time intervals is straightforward: the reach-set over $[t_0, t] \subseteq [0, T]$ is

$$\mathcal{R}^e(\mathcal{X}_0, [t_0, t]) := \{\varphi(\mathbf{x}_0, s) : \mathbf{x}_0 \in \mathcal{X}_0, \forall s \in [t_0, t]\}. \quad (28)$$

The difference between reach-sets for time points and for time intervals is that the former are evaluated at a particular time t , while the latter include *all* states reachable for *any* time between t_0 and t , hence $\mathcal{R}^e(\mathcal{X}_0, t) \subseteq \mathcal{R}^e(\mathcal{X}_0, [t_0, t])$. Finally, given a time step $\delta > 0$ and a collection of reach-sets $\{\mathcal{R}^e(\mathcal{X}_0, [\delta(k-1), \delta k])\}_{k=1}^N$ with $N = T/\delta$, the *flowpipe* of Eq. (26) is the set union,

$$\mathcal{F}^e(\mathcal{X}_0, [0, T]) := \bigcup_{k=1}^N \mathcal{R}^e(\mathcal{X}_0, [\delta(k-1), \delta k]). \quad (29)$$

In Eqs. (27)-(29), the superindex e is used to remark that the definitions refer to the *exact* or true sets. In practice, reachable sets can only be obtained approximately and several algorithms to numerically approximate reachable sets are known in the literature. Different methods crucially depend on how the sets are represented and the cost of operating with those representations.

2.3.3. Set representations

Three common set representations used in reachability analysis of linear systems are zonotopes, hyperrectangles and support functions. Let us briefly recall their definition.

Zonotopes. Given a vector $\mathbf{c} \in \mathbb{R}^n$ that we call *center* and a list of $p \geq n$ vectors that we call *generators*, $\mathbf{g}_1, \dots, \mathbf{g}_p$, $\mathbf{g}_i \in \mathbb{R}^n$, the associated zonotope is the set

$$Z = \left\{ \mathbf{x} \in \mathbb{R}^n : \mathbf{x} = \mathbf{c} + \sum_{i=1}^p \xi_i \mathbf{g}_i, \quad \xi_i \in [-1, 1] \right\}. \quad (30)$$

In compact notation we write $Z = \langle \mathbf{c}, \mathbf{G} \rangle_Z$, where each generator is stored as a column of the generators matrix $\mathbf{G} \in \mathbb{R}^{n \times p}$. Zonotopes can be interpreted in different ways, such as the Minkowski sum of line segments, or as the affine map of a unit ball in the infinity norm. The zonotope representation has been successfully used in reachability analysis because it offers a very compact representation relative to the number of vertices or faces, so it is well suited to represent high dimensional sets (Girard et al., 2006a).

Hyperrectangles. Given vectors $\mathbf{c} \in \mathbb{R}^n$ and $\mathbf{r} \in \mathbb{R}^n$ that we call *center* and *radius* respectively, the associated hyperrectangle is the set

$$H = \{ \mathbf{x} \in \mathbb{R}^n : |x_i - c_i| \leq r_i, \quad i = 1, \dots, n \}. \quad (31)$$

In compact notation we write $H = \langle \mathbf{c}, \mathbf{r} \rangle_H$. Every hyperrectangle is a zonotope but the converse is not true. In fact, the linear map of a hyperrectangle can be (exactly) represented as a zonotope. While computations with hyperrectangles can be performed very efficiently, using hyperrectangles for reachability can result in coarse overapproximations unless they are used in concurrence with other representations at intermediate parts of the algorithm.

Support functions. The support function of a set $X \subset \mathbb{R}^n$ along direction $\mathbf{d} \in \mathbb{R}^n$ is the scalar

$$\rho(\mathbf{d}, X) = \max_{\mathbf{x} \in X} \mathbf{d}^T \mathbf{x}, \quad (32)$$

where the superscript T denotes transposition. The set of points in X that are the maximizers of Eq. (32) are called the *support vectors*. The intuition behind Eq. (32) is that support functions represent the farthest (signed) distance to the origin of the set X along direction \mathbf{d} . Given that the direction can be chosen at will, support functions can be used to obtain the solution corresponding to a linear combination of the state variables at once and at a reduced cost (Le Guernic, 2009).

3. Methodology

Consider the following system of differential equations:

$$\mathbf{M}\ddot{\mathbf{u}}(t) + \mathbf{C}\dot{\mathbf{u}}(t) + \mathbf{K}\mathbf{u}(t) = \mathbf{f}(t), \quad \mathbf{u}(0) \in \mathcal{U}_0, \dot{\mathbf{u}}(0) \in \mathcal{V}_0 \quad t \in [0, T], \quad (33)$$

with state vector $\mathbf{u}(t) \in \mathbb{R}^m$ and where $\mathcal{U}_0 \subset \mathbb{R}^m$ and $\mathcal{V}_0 \subset \mathbb{R}^m$ are the sets of initial values for \mathbf{u} and $\dot{\mathbf{u}}$ (if provided), respectively. This system of equations can be interpreted as a general representation of a heat transfer or structural dynamics problem. In Eq. (33) \mathbf{M} , \mathbf{C} , and \mathbf{K} are square $m \times m$ matrices and $\mathbf{f}(t)$ is an m -dimensional vector-valued function that we generically call *input*.

Let us outline the methodology used to compute reachable states in an exhaustive (or conservative) way. The algorithm can be summarized as follows:

- (i) **Homogeneization and transformation to first order.** Transform the system in Eq. (33) into a system of linear homogeneous ODEs of first order as in Eq. (26) using the method described in Section 3.1.
- (ii) **Conservative time discretization.** Build a set $\Omega_0 \subset \mathbb{R}^n$ that contains all exact trajectories between time 0 and time $\delta > 0$, i.e. satisfying the property:

$$\Omega_0^e := \mathcal{R}^e(\mathcal{X}_0, [0, \delta]) \subseteq \Omega_0. \quad (34)$$

- (iii) **Set propagation.** Set the initial set $X_0 := \Omega_0$ and the state transition matrix $\Phi := e^{\mathbf{A}\delta}$, and solve the set-based recurrence

$$X_{k+1} = \Phi X_k, \quad X_0 \subset \mathbb{R}^n, \quad k = 0, 1, \dots, N-2. \quad (35)$$

By construction it is guaranteed that $\mathcal{R}^e(\mathcal{X}_0, [\delta(k-1), \delta k]) \subseteq X_{k-1}$ for all $k = 1, \dots, N$. In the rest of this section we elaborate on each sub-step of the method. Section 3.1 deals with homogeneization, Section 3.2 with time discretization, and Section 3.3 with details on different algorithms for set propagation whose choice depends on the type of solid mechanics problem considered.

3.1. Homogeneization and transformation to first order

We now describe an algebraic transformation of the governing equations used as a pre-processing step in our algorithm. The idea is to transform second order systems of the form (33) into a

first order, homogeneous system. Not every second order equation of motion can be cast into $\dot{\mathbf{x}}(t) = \mathbf{A}\mathbf{x}(t)$; however, under some assumptions and for certain classes of input functions $\mathbf{f}(t)$, such transformation is possible if we introduce auxiliary variables. Input uncertainty is modeled in set-valued initial states, and variations in time are allowed by specifying the right-hand side of the auxiliary variables associated to inputs. Details are given in the following paragraphs.

3.1.1. Homogeneization

Let us consider that the inputs vector $\mathbf{f}(t)$ can be decomposed as follows:

$$\mathbf{f}(t) = \sum_{i=1}^{n_f} \mathbf{f}_0^{(i)} \eta^{(i)}(t), \quad (36)$$

where n_f is the number of input components, each $\mathbf{f}_0^{(i)} \in \mathbb{R}^m$ is a known vector and the functions $\eta^{(i)}(t) : [0, T] \rightarrow \mathbb{R}$ are functions that can be expressed in terms of the solution of a first order homogeneous system of differential equations.

The property of the functions $\eta^{(i)}$ can be written as follows: for each function $\eta^{(i)}$ there exists a vector of $q^{(i)}$ functions $\boldsymbol{\xi}^{(i)}(t) = [\xi_1^{(i)}(t), \dots, \xi_{q^{(i)}}^{(i)}(t)]^T$, such that for each $i = 1, \dots, n_f$,

$$\begin{cases} \eta^{(i)}(t) = \xi_1^{(i)}(t) \\ \dot{\boldsymbol{\xi}}^{(i)}(t) = \mathbf{B}^{(i)} \boldsymbol{\xi}^{(i)}(t) \end{cases} \quad (37)$$

where $\mathbf{B}^{(i)}$ is a $q^{(i)} \times q^{(i)}$ matrix. Special cases of these input functions are constant or exponential functions (with $q = 1$) and trigonometric functions (with $q = 2$). Using Eq. (37) into Eq. (36), we can reformulate Eq. (33) as

$$\begin{cases} \mathbf{M}\ddot{\mathbf{u}}(t) + \mathbf{C}\dot{\mathbf{u}}(t) = -\mathbf{K}\mathbf{u}(t) + \sum_{i=1}^{n_f} \mathbf{f}_0^{(i)} \xi_1^{(i)}(t) \\ \dot{\boldsymbol{\xi}}^{(i)}(t) = \mathbf{B}^{(i)} \boldsymbol{\xi}^{(i)}(t) \quad i = 1, \dots, n_f \end{cases} \quad (38)$$

obtaining then an homogeneous system of differential equations with $m + \sum_{i=1}^{n_f} q^{(i)}$ unknowns. Finally a matrix form is considered for the input terms

$$\begin{cases} \mathbf{M}\ddot{\mathbf{u}}(t) + \mathbf{C}\dot{\mathbf{u}}(t) = -\mathbf{K}\mathbf{u}(t) + \sum_{i=1}^{n_f} \mathbf{F}_0^{(i)} \boldsymbol{\xi}^{(i)}(t) \\ \dot{\boldsymbol{\xi}}^{(i)}(t) = \mathbf{B}^{(i)} \boldsymbol{\xi}^{(i)}(t) \quad i = 1, \dots, n_f \end{cases} \quad (39)$$

where

$$\mathbf{F}_0^{(i)} = \left[\mathbf{f}_0^{(i)} \mid \mathbf{0}_{m \times (q^{(i)} - 1)} \right].$$

3.1.2. Coupled formulation and transformation to first order

The system of differential equations in Eq. (39) can be written in a first order matrix coupled form as follows:

$$\frac{d}{dt} \begin{bmatrix} \mathbf{x}(t) \\ \boldsymbol{\xi}^{(1)}(t) \\ \vdots \\ \boldsymbol{\xi}^{(n_f)}(t) \end{bmatrix} = \mathbf{A} \begin{bmatrix} \mathbf{x}(t) \\ \boldsymbol{\xi}^{(1)}(t) \\ \vdots \\ \boldsymbol{\xi}^{(n_f)}(t) \end{bmatrix}, \quad (40)$$

where the unknowns $\mathbf{x}(t)$ are called *state variables* and the unknowns $\boldsymbol{\xi}^{(i)}(t)$ are called *input variables*. If \mathcal{X}_0 and \mathcal{C}_0 denote the initial condition for the state (resp. input) variables, the joint initial condition in Eq. (40) is the Cartesian product $\mathcal{X}_0 \times \mathcal{C}_0$. The form of the matrix \mathbf{A} depends whether the mass matrix \mathbf{M} in (33) is null (i) or not (ii):

- (i) If $\mathbf{M} = 0$ and \mathbf{C} is invertible, set $\mathbf{x} = \mathbf{u}$ and

$$\mathbf{A} = \left[\begin{array}{c|c|c|c} -\mathbf{C}^{-1}\mathbf{K} & -\mathbf{C}^{-1}\mathbf{F}_0^{(1)} & \dots & -\mathbf{C}^{-1}\mathbf{F}_0^{(n_f)} \\ \hline \mathbf{0} & \mathbf{B}^{(1)} & \mathbf{0} & \mathbf{0} \\ \hline \vdots & \mathbf{0} & \ddots & \mathbf{0} \\ \hline \mathbf{0} & \dots & \mathbf{0} & \mathbf{B}^{(n_f)} \end{array} \right], \quad (41)$$

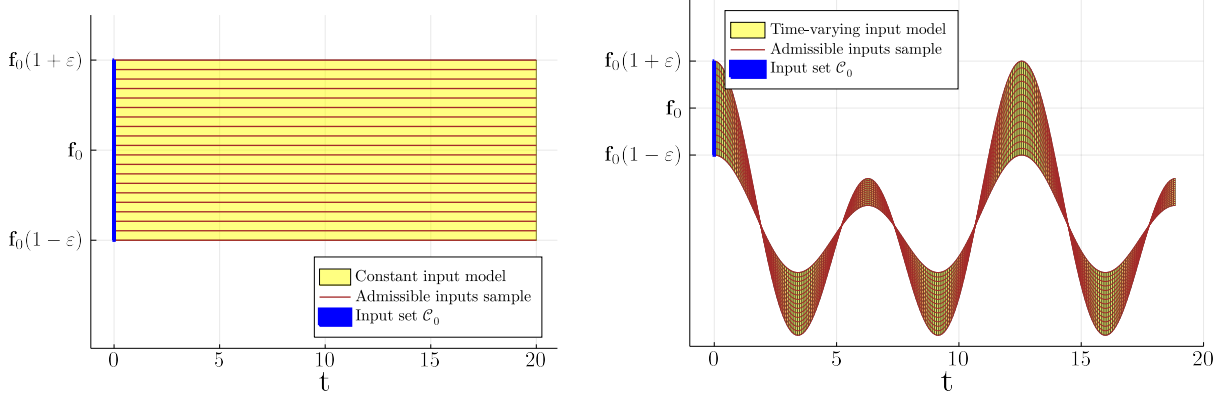
and the initial set for the state variables is $\mathcal{X}_0 = \mathcal{U}_0$.

- (ii) If $\mathbf{M} \neq 0$ and it is invertible, we introduce the $2m$ -dimensional state vector $\mathbf{x} = (\mathbf{u}, \dot{\mathbf{u}})^T$, and \mathbf{A} is given by:

$$\mathbf{A} = \left[\begin{array}{c|c|c|c|c} \mathbf{0} & \mathbf{I} & \mathbf{0} & \dots & \mathbf{0} \\ \hline -\mathbf{M}^{-1}\mathbf{K} & -\mathbf{M}^{-1}\mathbf{C} & -\mathbf{M}^{-1}\mathbf{F}_0^{(1)} & \dots & -\mathbf{M}^{-1}\mathbf{F}_0^{(n_f)} \\ \hline \mathbf{0} & \mathbf{0} & \mathbf{B}^{(1)} & \mathbf{0} & \mathbf{0} \\ \hline \vdots & \vdots & \mathbf{0} & \ddots & \mathbf{0} \\ \hline \mathbf{0} & \mathbf{0} & \dots & \mathbf{0} & \mathbf{B}^{(n_f)} \end{array} \right], \quad (42)$$

and in this case, the initial condition for the state variables is the Cartesian product $\mathcal{X}_0 := \mathcal{U}_0 \times \mathcal{V}_0$.

Concerning the initial condition for the input variables in Eq. (40), that we call \mathcal{C}_0 , they are not restricted to be a single value; in fact they can be chosen to be e.g. a hyperrectangle, in which case



(a) Example of constant input model with an uncertain interval \mathcal{C}_0 . (b) Example of time-varying input model with two contributions, $\xi_1^{(1)}(t) = \cos(t)$ and $\xi_1^{(2)}(t) = \frac{5}{9} \cos(t/2)$.

Figure 5: Illustration of different input function assumptions. A set \mathcal{C}_0 is used to span all possible input functions with the specified behavior; a uniform sample is shown for each case.

we can model an uncertainty of the initial conditions around nominal values for a whole family of input functions, with a single flowpipe computation.

To illustrate the formulation in a simple example, assume that there is only one constant forcing term \mathbf{f}_0 ($n_f = 1$, $\mathbf{B}^{(1)} = \mathbf{0}_{1 \times 1}$), and that we take an interval $\mathcal{C}_0 = [1 - \varepsilon, 1 + \varepsilon] \subset \mathbb{R}$ for some $\varepsilon > 0$. With this initial condition, we can model all forcing functions that take any constant value within $\mathbf{f}_0 \pm \varepsilon \mathbf{f}_0$, as shown in Fig. 5a. In Fig. 5b we show a more general example that combines two time-varying input functions. The three-dimensional heat transfer problem in Example 4 of Section 4.4 combines three different input terms.

3.2. Conservative time discretization

In this section we explain how to perform a time discretization that is conservative in the sense of including all admissible behaviors in dense time, and continue with the description of different methods to propagate such initial set according to the system's state transition matrix.

We recall that \mathcal{X}_0 is the set of initial states and, since the analytic solution of Eq. (26) at $t = \delta$ is $\varphi(\mathbf{x}_0, \delta) = \Phi \mathbf{x}_0$ for each $\mathbf{x}_0 \in \mathcal{X}_0$, then $\Phi \mathcal{X}_0$ is the set of transformed states after one time increment of size δ , i.e. $\mathcal{R}^e(\mathcal{X}_0, \delta) = \Phi \mathcal{X}_0$. The reach-set for the time interval $[0, \delta]$ is more difficult to obtain because there is no closed-form expression. Let $CH(X, Y)$ denote the *convex hull* of the set union of two sets $X \subseteq \mathbb{R}^n$, $Y \subseteq \mathbb{R}^n$, i.e. the smallest convex set that contains X and Y , defined

by

$$CH(X, Y) = \{z \in \mathbb{R}^n : z = \lambda x + (1 - \lambda)y, \quad \lambda \in [0, 1], \quad x \in X, \quad y \in Y\}. \quad (43)$$

It is clear (compare e.g. with Fig. 3a) that the analytic solution does not follow the straight line of the convex hull $CH(\mathcal{X}_0, \Phi\mathcal{X}_0)$ for intermediate times between 0 and δ , because trajectories curve due to the system's dynamics. Hence we need to enlarge, or bloat, the convex hull by a suitable amount such that all the exact reachable states Ω_0^e are covered.

To obtain a set Ω_0 satisfying Eq. (34), we propose a slight variation of the method presented in (Frehse et al., 2011). The advantage of the new method is that it doesn't require to solve an optimization problem for each direction of interest. The symbol $\square(\mathcal{X})$ represents the symmetric interval hull of $\mathcal{X} \subset \mathbb{R}^n$, that is the smallest hyperrectangle centered at the origin that contains \mathcal{X} .

Proposition 1. *Define the following pair of sets*

$$\Omega_0^+ = CH(\mathcal{X}_0, \Phi\mathcal{X}_0 \oplus E^+(\mathbf{A}, \mathcal{X}_0, \delta)) \quad (44)$$

$$\Omega_0^- = CH(\Phi\mathcal{X}_0, \mathcal{X}_0 \oplus E^+(\mathbf{A}, \Phi\mathcal{X}_0, \delta)) \quad (45)$$

where $E^+(\mathbf{A}, \mathcal{X}_0, \delta) = \square(\mathbf{P}(|\mathbf{A}|, \delta) \square(\mathbf{A}^2\mathcal{X}_0))$ and $\mathbf{P}(\mathbf{A}, \delta) = \sum_{i=0}^{\infty} \mathbf{A}^i \delta^{i+2} / (i+2)!$. Then, the set $\Omega_0 := \Omega_0^+ \cap \Omega_0^-$ encloses Ω_0^e , i.e. $\Omega_0^e \subseteq \Omega_0$. Moreover, $\Omega_0 \rightarrow \Omega_0^e$ as $\delta \rightarrow 0$.

The proof of Prop. 1 is left to Appendix A. The intuition behind Prop. 1 is that first Eq. (44) performs one step forward in time (from $t = 0$ to $t = \delta$) with a bloating set E^+ that is a small box around the origin (E^+ tends to zero as $\delta \rightarrow 0$), and second, Eq. (45) performs one step in reverse time (from $t = \delta$ to $t = 0$) which are then intersected to remove spurious overapproximation errors.

The result in our running example is shown in Fig. 3a: note how the set Ω_0 (orange) encloses the exact (curved) solution for all intermediate times between 0 and δ . The case depicted in Fig. 4a is more interesting: it corresponds to the case in which the set of initial states \mathcal{X}_0 is a hyperrectangle. While the obtained set Ω_0 (orange) may not be the tightest convex set containing the exact reachable set Ω_0^e , it is nonetheless a very good approximation. Finally, let us remark that Ω_0 is in general a polygon (or a polytope in higher dimensions). In practice, either we approximate it with a hyperrectangle (see Fig. 4a in lightblue), or use lazy (i.e. on-demand) evaluations of the support function. While the former approach leads to faster runtimes for large time horizons, the latter does not introduce additional overapproximation error. The hyperrectangular approximation of Ω_0 can be easily computed using support functions.

Having obtained the set Ω_0 to fulfill the conservative time discretization requirement in Eq. (34), we proceed in the next paragraphs to explain the set-based propagation of the sequence. To solve Eq. (35), three different approaches are presented: zonotopes, hyperrectangles and support functions. Each method offers a different efficiency vs accuracy tradeoff and scales differently with the system's dimension. For Section 4 we have selected the method that is more suitable for each problem. A complete evaluation of the different methods is out of the scope of this article (see also (Althoff et al., 2020a) for a comparison of results obtained by different software tools on a set of benchmark problems).

3.3. Set propagation

3.3.1. Set propagation using zonotopes

To solve the set-based recurrence of Eq. (35) using zonotopes, it suffices to observe that zonotopes are closed under linear maps: $\mathbf{M}Z = \langle \mathbf{M}\mathbf{c}, \mathbf{M}\mathbf{G} \rangle_Z$ is again a zonotope for any $\mathbf{M} \in \mathbb{R}^{m \times n}$, obtained by transforming the center and generators of Z by the linear map \mathbf{M} . Therefore if $Z_0 = \langle \mathbf{c}_0, \mathbf{G}_0 \rangle_Z$ is a zonotope, it holds that

$$Z_k = \langle \Phi^k \mathbf{c}_0, \Phi^k \mathbf{G}_0 \rangle_Z, \quad k = 0, 1, \dots, N-1. \quad (46)$$

In general, the initial set Ω_0 from Prop. 1 is not a zonotope so we overapproximate it with a hyperrectangle as a pre-processing step. Set propagation using zonotopes is illustrated in Fig. 3b for singleton resp. in Fig. 4b for distributed initial conditions (light-green).

Finally we remark that, in a simplified model of computation, the time complexity of Eq. (46) is $\mathcal{O}(Nn^2p)$, and the space complexity is $\mathcal{O}(Nnp)$. Typically, $p = n$ hence storing all intermediate zonotopes can be expensive if the state-space dimension n is sufficiently large. However, there are situations in which we are only interested in obtaining minimum and maximum bounds of the flowpipe and in that case it is more efficient and equally accurate to propagate axis-aligned hyperrectangles. This is the subject of the next subsection.

3.3.2. Set propagation using hyperrectangles

Hyperrectangular approximations are particularly useful in problems where it is relevant to find the maximum or minimum values of all the state variables; for example in the longitudinal oscillations of a bar if we are interested in computing the maximum displacements and velocities

(cf. Example 4.2), or in a massive concrete structure model we may be interested in the maximum temperature achieved at any mesh point (cf. Example 4.4).

Given a zonotope Z , we say that H is a *tight* hyperrectangular approximation if H is the smallest hyperrectangle that contains Z . The following proposition formalizes the idea of approximating the zonotope flowpipe with tight hyperrectangles.

Proposition 2. *Let $H_0 = \langle \mathbf{c}_0, \mathbf{r}_0 \rangle_H$ be a hyperrectangle enclosing Ω_0^e . For each $k \geq 1$, define the sequence $\mathbf{c}_k = \Phi^k \mathbf{c}_0$ and $\mathbf{r}_k = |\Phi^k| \mathbf{r}_0$, where the absolute values are taken component-wise. Then, the sequence of hyperrectangles $H_k = \langle \mathbf{c}_k, \mathbf{r}_k \rangle$ tightly overapproximates the solutions of the recurrence (35) for all $k = 0, \dots, N - 1$.*

The proof of Prop. 2 is left to Appendix B. Concerning the computational cost, the time complexity of the method in Prop. 2 is $\mathcal{O}(Nn^2)$, and the space complexity is $\mathcal{O}(Nn)$. Note that computing with hyperrectangles is comparatively less expensive than zonotopes, although the latter have more expressive power than the former.

Set propagation using hyperrectangles is illustrated in Fig. 3b for singleton initial conditions resp. in Fig. 4b for distributed initial conditions (light-blue). For the 6th reach-set the hyperrectangle and the zonotope coincide; in general though, the hyperrectangle encloses the zonotope. However, for the k -th reach-set, the maximum and minimum of Z_k are always the same to those obtained with H_k as claimed in Prop. 2.

While solving Eq. (35) using hyperrectangles scales very well with the dimension, this approach is limited to obtaining maximum (resp. minimum) values over solutions. We can interpret such computation as the maximum of the scalar product $\mathbf{d}^T \mathbf{x}(t)$ over all $\mathbf{x}(t) \in \mathcal{R}^e(\mathcal{X}_0, [\delta(k-1), \delta k])$, where \mathbf{d} is any canonical direction of \mathbb{R}^n , i.e. of the form $\mathbf{d} = (0, \dots, 1, \dots, 0)^T$. The minimum can be obtained analogously. Using support functions, as explained in the next section, we can generalize the computation for an arbitrary direction $\mathbf{d} \in \mathbb{R}^n$.

3.3.3. Set propagation using support functions

The first systematic attempt to solve Eq. (35) using support functions was presented in (Le Guernic & Girard, 2010). The idea is to make use of the property $\rho(\mathbf{d}, \mathbf{M}X) = \rho(\mathbf{M}^T \mathbf{d}, X)$ for any matrix $\mathbf{M} \in \mathbb{R}^{n \times n}$. By successive application of this rule,

$$\rho(\mathbf{d}, X_k) = \rho((\Phi^T)^k \mathbf{d}, X_0), \quad k = 0, 1, \dots, N - 1. \quad (47)$$

The support function of common set representations (e.g. hyperrectangles and zonotopes) is known analytically so in those cases it can be computed very efficiently. In addition, the support function of an intersection satisfies that $\rho(\mathbf{d}, X \cap Y) \leq \min\{\rho(\mathbf{d}, X), \rho(\mathbf{d}, Y)\}$, while for the case of Minkowski sums, $\rho(\mathbf{d}, X \oplus Y) = \rho(\mathbf{d}, X) + \rho(\mathbf{d}, Y)$.

Using support functions we can compute linear combinations of the state variables, i.e. we can solve the recurrence (35) *along a given direction* directly solving a recurrence for the support function, instead of computing the flowpipe for all variables and then extracting the relevant information. A practical application of the solution method in Eq. (47) to obtain the spatial gradient in a heat transfer problem is presented in Example 4.3.

4. Numerical results

In order to obtain comparative results about the performance and accuracy of the methods discussed, four numerical examples are solved. Each example introduces a new motivation and level of complexity in the comparative process of the methods.

The reachability problems are solved using the JuliaReach library (Forets et al., 2021; Bogomolov et al., 2019), implemented in the Julia language (Bezanson et al., 2017). The computations associated to the Finite Element Method are done using source code from the ONSAS library (Pérez Zerpa et al., 2021) implemented in GNU-Octave (Eaton et al., 2020). The visualization is done using JuliaPlots (Breloff et al., 2021) and Paraview (Ahrens et al., 2005). All the results are executed in a laptop computer running Linux OS, with an Intel(R) Core(TM) i7-8705G CPU, 3.10GHz processor and 16GB RAM.

4.1. Example 1: accuracy analysis of the harmonic oscillator

In this example, the one-dimensional harmonic oscillator presented in Section 2.3.1 is considered. We compare the set propagation results in terms of accuracy with respect to reference numerical integration methods and the analytic solution.

4.1.1. Problem definition

The governing equation is given in Eq. (24) and the parameters considered are frequency $\omega = 4\pi$ (i.e. period 0.5 s), and initial conditions $u(0) = 1$, $\dot{u}(0) = v(0) = 0$. Different time steps are considered: $\delta = 0.025$ s and $\delta = 0.05$ s.

4.1.2. Numerical resolution

The results obtained using time step $\delta = 0.025$ s are shown in Figure 6. The solution obtained using the Newmark method is shown with red circles, the solution using the Bathe method is represented by green triangles and the analytic solution is represented by a solid magenta line. Regarding the solution obtained by set propagation, we represent the flowpipe using polygons and show their projection onto the $u(t)$ axis using light-blue boxes.

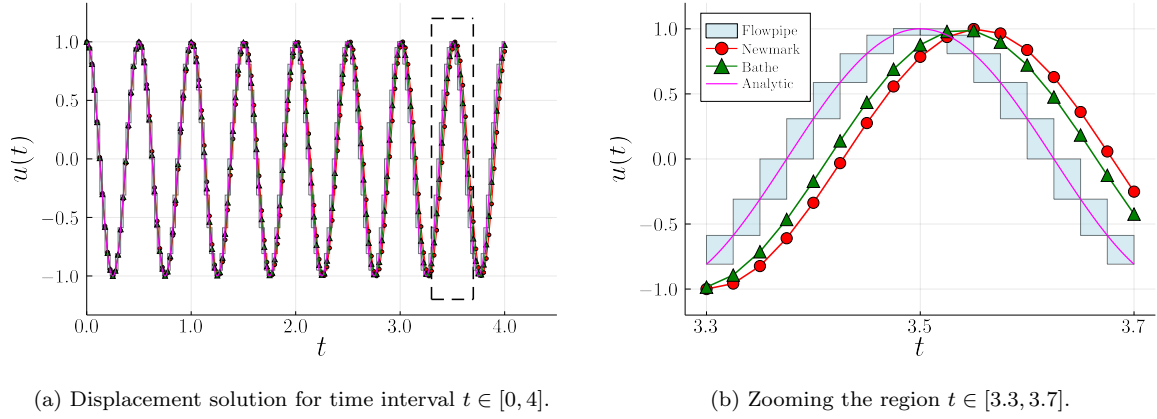


Figure 6: Example 1: displacements obtained using $\alpha = \delta/T = 0.05$. The analytic solution (magenta) is shown superposed with the numerical solution obtained with Newmark's method (red circles) and Bathe's method (green triangles).

In Figure 6b it can be observed that the analytic solution is contained in the flowpipe. On the other hand, the numerical methods show a considerable period elongation (after 7 periods of simulation).

The results obtained using a larger time step $\delta = 0.05$ s are shown in Figure 7. In this case, in Figure 7b it can be observed a greater period elongation for the numerical methods. The flowpipe still includes the analytic solution but the width of the intervals on the $u(t)$ axis is larger than in the previous case.

4.1.3. Accuracy analysis

Accuracy analysis of numerical integration methods can be done using two tools: Period Elongation (*PE*) and Amplitude Decay (*AD*) (Bathe & Noh, 2012; Bathe, 2014). In this section we compute these magnitudes for the numerical results obtained and draw a comparison with respect to the set propagation method. The numerical data used to compute these magnitudes corresponds

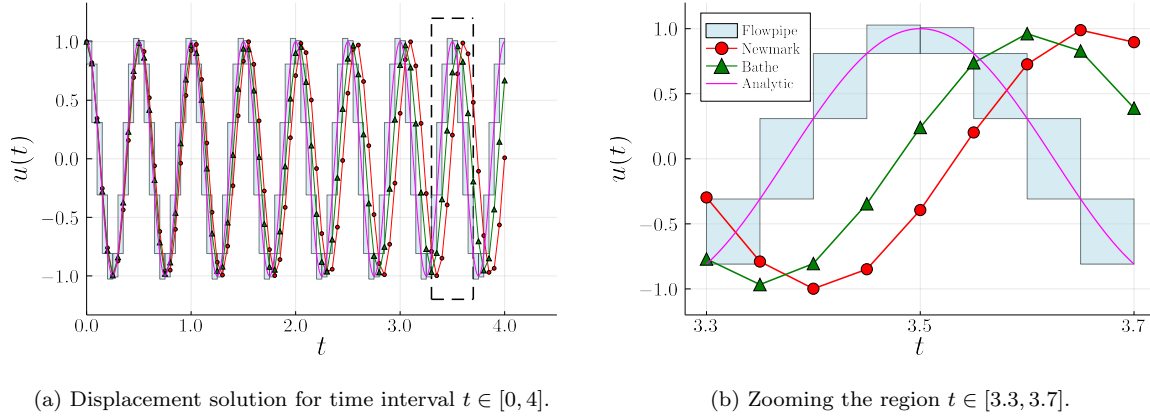


Figure 7: Example 1: displacements using $\alpha = \delta/T = 0.1$. The analytic solution (magenta) is shown superposed with the numerical solution obtained with Newmark’s method (red circles) and Bathe’s method (green triangles).

to a simulation for 50 periods, i.e. 25 seconds.

The PE can be computed using the following expression:

$$PE = \frac{T_{num} - T_{nat}}{T_{nat}}, \quad (48)$$

where T_{nat} is the natural period of the oscillator and T_{num} is the period of the numerical solution. For the numerical integration methods, we compute T_{num} using standard spectral analysis methods. On the other hand, to our knowledge there are no methods for the computation of PE estimates of flowpipes, thus we devised a procedure to compute T_{num} in the set-based setting. The notions used in the method are presented in Appendix C, where both PE and AD estimations are described.

In Fig. 8a the PEs computed for the Bathe, Newmark and set propagation methods are presented, where the latter is shown in blue squares and the Bathe and Newmark methods using triangles and circles, respectively. The values of α considered are intended to reproduce the results shown in (Bathe, 2014). It can be seen that Newmark and Bathe methods present PE values, that match with literature results, while the set propagation results do not present PE.

The numerical amplitude A_{num} after n_A periods is $A_{num} = A(1 - AD)^{n_A}$, hence the Amplitude Decay AD is:

$$AD = 1 - \left(\frac{A_{num}}{A} \right)^{\frac{1}{n_A}}. \quad (49)$$

In Fig. 8b the computed values of AD are shown. As it is expected, the Newmark method does not present AD while the Bathe method presents a curve that matches the literature results. The set propagation method has not significant AD, with values below 0.15% for any α .

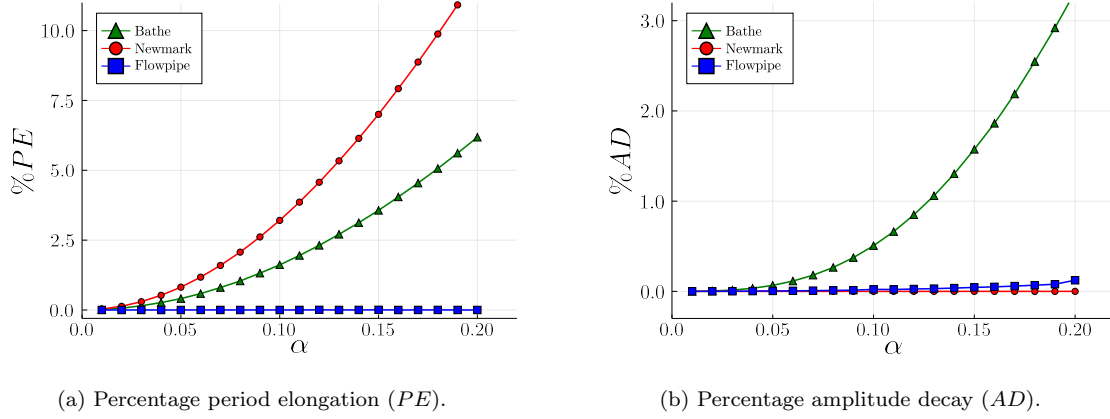


Figure 8: Example 1: PE and AD as a function of the relative step size $\alpha = \delta/T$. In red (green) color, the results for Newmark (Bathe) methods. In blue, the results obtained with the set propagation approach.

The results obtained show that the set propagation method presents advantages with respect to the numerical integration methods, in terms of PE, and competitive results in terms of AD. The set propagation method presents good results for single degree of freedom problems. In the following example, the problem is extended to increase the number of unknowns.

4.2. Example 2 - Clamped-Free Bar

We consider a uni-dimensional wave propagation problem from (Malakiyeh et al., 2019). The purpose of this example is to evaluate the conservative time integration scheme for single initial conditions in a high-dimensional problem. Subsequent examples consider variations in the initial conditions and input parameters.

4.2.1. Problem definition

The domain consists of a bar of length $L = 200$ and cross-section area $A = 1$, formed by a linear elastic material with Young modulus $E = 30 \times 10^6$ and density $\rho = 7.3 \times 10^{-4}$. The free end of the bar is submitted to a step force $F(t) = 10,000H(t)$, where $H(t)$ is the Heaviside function. The bar is governed by the partial differential equation

$$EA \frac{\partial^2 u}{\partial x^2}(x, t) - \rho A \frac{\partial^2 u}{\partial t^2}(x, t) = 0, \quad (50)$$

where $u(x, t)$ is the displacement of the point in position x at time t , considering the axis shown in Fig. 9.

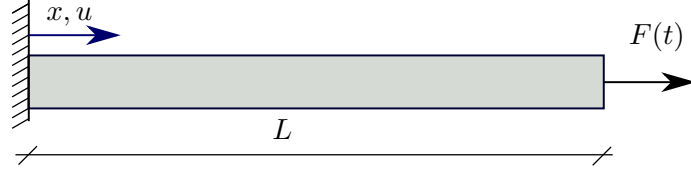


Figure 9: Example 2: diagram of the clamped-free bar excited by end load.

The bar is considered to be initially at rest, with $u(x, 0) = 0$ and $\dot{u}(x, 0) = 0$ for all $x \in [0, L]$. The boundary conditions are $u(0, t) = 0$, corresponding to the fixed end, and $\sigma(L, t)A = F(t)$, for the free end, where $\sigma(x, t) = E \frac{\partial u}{\partial x}(x, t)$ is the stress function at point x and time t .

The analytical solution of this problem in the continuum domain can be obtained using mode superposition (Géradin & Rixen, 2014), and it is given by:

$$u(x, t) = \frac{8FL}{\pi^2 EA} \sum_{s=1}^{\infty} \left\{ \frac{(-1)^{s-1}}{(2s-1)^2} \sin \frac{(2s-1)\pi x}{2L} \left(1 - \cos \frac{(2s-1)\pi \mu t}{2L} \right) \right\}, \quad (51)$$

where $\mu = \sqrt{E/\rho}$.

4.2.2. Numerical resolution

The numerical space discretization is done considering $N = 1000$ two-node finite elements with linear interpolation. The following $N \times N$ mass and stiffness matrices are obtained:

$$\mathbf{K} = \frac{EA}{\ell} \begin{bmatrix} 2 & -1 & & & 0 \\ -1 & 2 & -1 & & \\ & -1 & 2 & \ddots & \\ & & \ddots & \ddots & -1 \\ & & & -1 & 2 & -1 \\ 0 & & & & -1 & 1 \end{bmatrix}, \quad \mathbf{M} = \frac{\rho A \ell}{2} \begin{bmatrix} 2 & & & & 0 \\ & 2 & & & \\ & & 2 & & \\ & & & \ddots & \\ & & & & 2 \\ 0 & & & & & 1 \end{bmatrix},$$

where $\ell = L/N$ is the length of each element. The damping matrix \mathbf{C} in Eq. (8) is an $N \times N$ matrix with zeros.

The displacements obtained for node 700 are shown in Fig. 10 and in Fig. 11 a zoom at time 5.6×10^{-3} is shown. In this case we present both the analytical solution in the continuum and the analytical solution in the discrete domain. The flowpipe computing using set propagation includes the analytic solution in the space-discretized domain, since that is the exact solution of the system of ODEs.

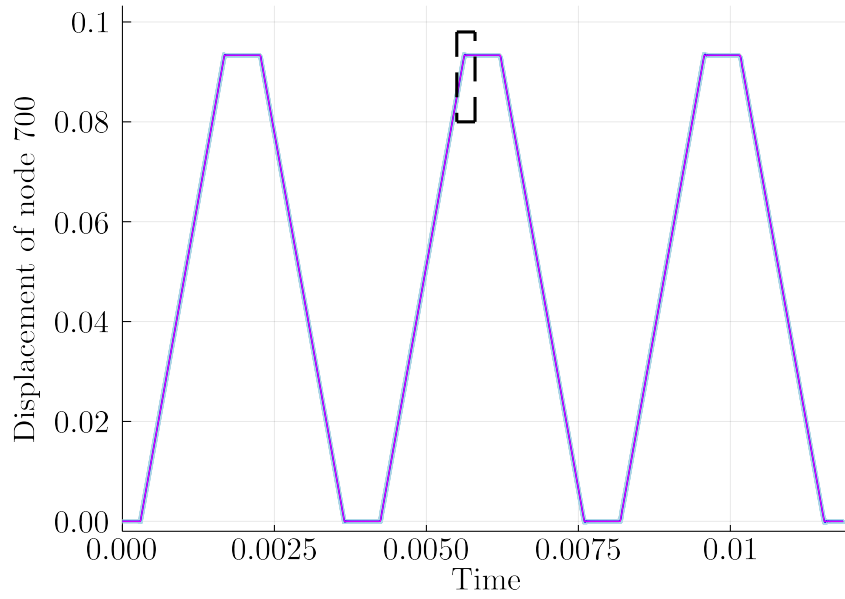


Figure 10: Example 2: Displacement of node 700 as a function of time corresponding to the analytic solution of the PDE (magenta), the analytic solution of the ODE (blue) and the flowpipe (light-blue). The rectangle shows the zoomed region.

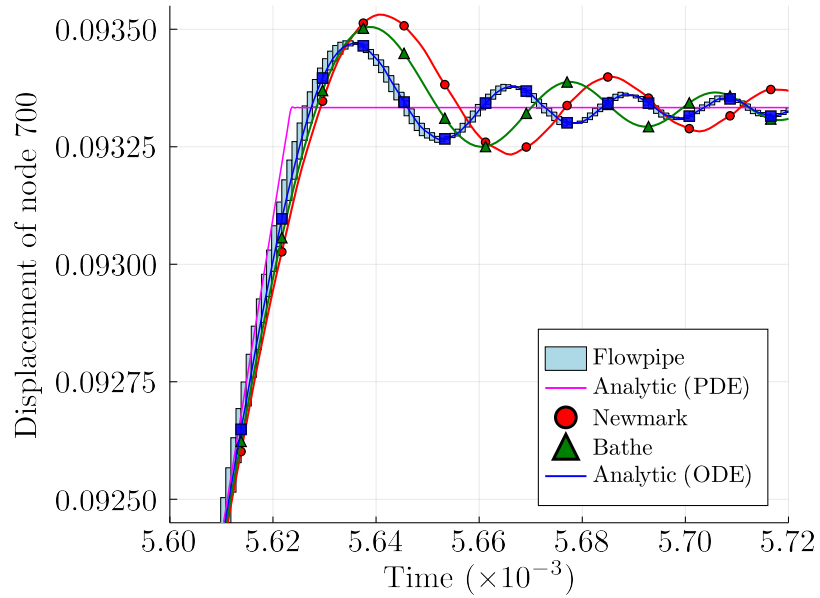


Figure 11: Example 2: Displacement of node 700 of the clamped beam model as a function of time.

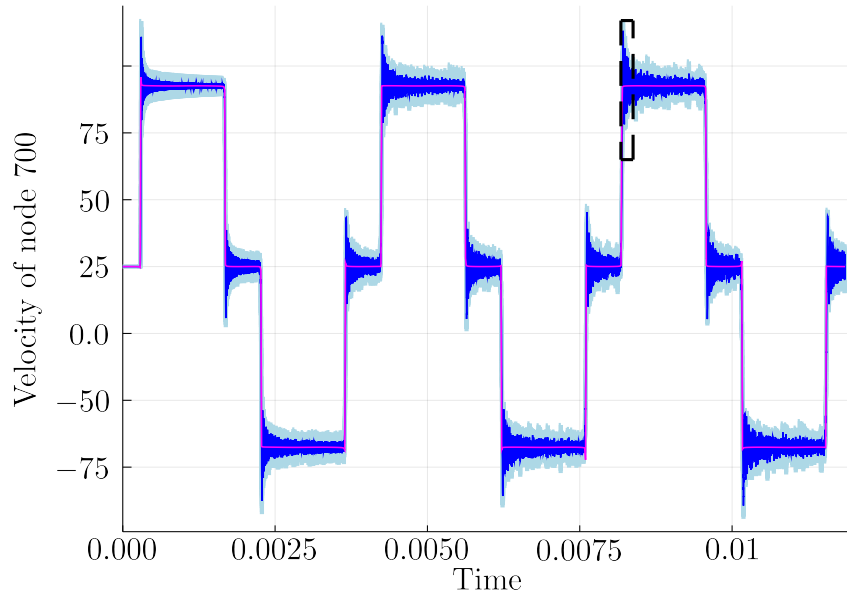


Figure 12: Example 2: velocity of node 700 as a function of time corresponding to the analytic solution of the PDE (magenta), the analytic solution of the ODE (blue) and the flowpipe (light-blue). The rectangle shows the zoomed region.

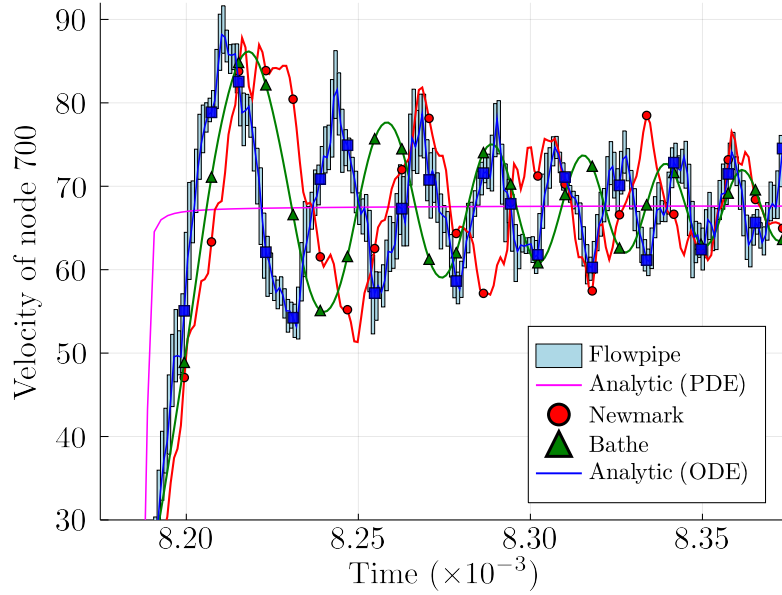


Figure 13: Example 2: zoom for the velocity of node 700.

In Fig. 12 the velocities obtained in node 700 are shown, and in Fig. 13 a zoom is shown. The analytical solution is again within the flowpipe, confirming the theoretically expected results. In this problem the flowpipe has been obtained using support functions along the node of interest and a box overapproximation of Ω_0 was used.

4.3. Example 3 - One-dimensional heat equation

In this example, a one-dimensional heat transfer problem is considered and interval sets are introduced for the initial values. The main goal of this problem is to evaluate the set propagation method as a tool to analyze the maximum temperature of a heat transfer problem under input uncertainty.

4.3.1. Problem definition

The domain consists of the interval $\Omega = [0, 1]$ and homogeneous Dirichlet boundary conditions are considered on both ends. The domain is assumed to have $\kappa = 1$ as thermal conductivity, $\rho = 1$ as density and $c = 1$ as specific heat capacity, all assumed uniform and constant.

The governing equations can be written as:

$$\begin{cases} \frac{\partial T(x, t)}{\partial t} = \frac{\kappa}{\rho c} \frac{\partial^2 T(x, t)}{\partial x^2}, & x \in \Omega \\ T(x, t) = 0, & x \in \{0, 1\}, \end{cases} \quad (52)$$

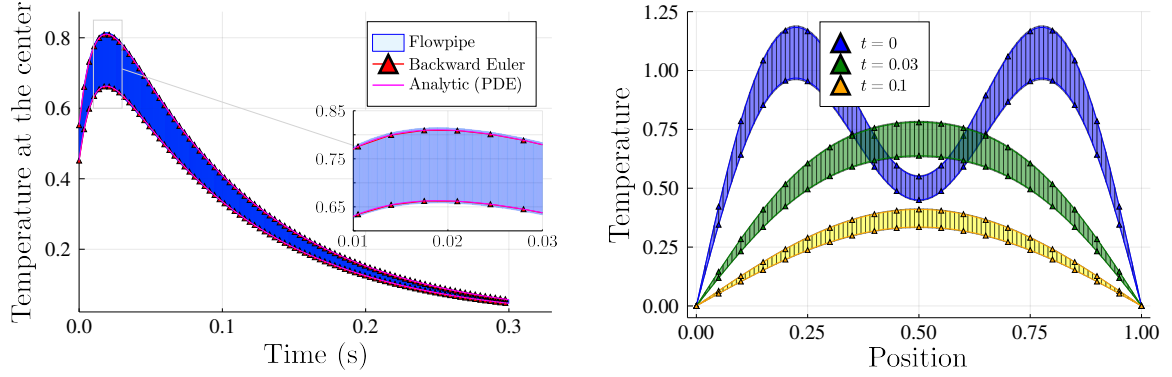
where $T(x, t)$ is the temperature in position x at time t .

For the initial conditions a set of possible temperature profiles is considered. The expression of the initial condition function is given by:

$$T(x, 0) = (1 + \varepsilon) \left(\sin(\pi x) + \frac{1}{2} \sin(3\pi x) \right), \quad \varepsilon \in [-0.1, 0.1], \quad (53)$$

where ε is a relative difference parameter associated with a given level of uncertainty in the initial values used for the simulations.

The Finite Element Method is used to discretize the governing equations considering a 100 two-node elements mesh with linear interpolation. It is important to remark that although the FEM discretization is used, the set of initial temperatures contains an infinite number of functions since ε belongs to an interval that is dense in \mathbb{R} .



(a) Temperature evolution obtained at the center node of the mesh ($x = 0.5$) using the analytic solution (magenta), the Backward Euler method for extreme cases (red triangle), and the set propagation method (blue flowpipe).

(b) Temperature profiles computed at different time points: $t = 0$ (blue), $t = 0.03$ (green) and $t = 0.1$ (yellow). Results from the Backward Euler method at extreme cases are shown using triangle markers.

Figure 14: Example 3: Results for the one-dimensional heat problem with set initial conditions obtained with the set propagation method and with the Backward Euler method.

4.3.2. Maximum temperature

The results obtained using the set propagation and the Backward Euler methods are compared with the analytic (exact) solution of Eq. (52). The time-step used for both resolution methods is $\delta = 10^{-5}$. In the case where set propagation is used, the entire set of parameters ε from Eq. (53) is considered, while for the Backward Euler method the analysis is only done for the two extreme cases: $\varepsilon = -0.1$ and $\varepsilon = 0.1$.

The results for the temperature in the node $x = 0.5$ are shown Fig. 14a and temperature profiles at times $t = 0$, 0.03 and $t = 0.10$ are shown in Fig. 14b. We compute the flowpipe using a hyperrectangle representation. Each direction corresponds to a different node. We observe that the flowpipe borders contain and tightly match the numerical solutions from the Backward Euler method and the analytical solutions starting from the two extreme initial conditions.

4.3.3. Maximum temperature gradient analysis

In this case, the goal of the analysis is to obtain the maximum value of the temperature gradients among all the points of the domain for all the feasible initial condition profiles.

A first order approximation of the flowpipe of the temperature gradient was obtained using support functions applied along certain diagonal template directions, as follows. Consider the temperature vector at time t , $\mathbf{T}(t) = [T_1(t), \dots, T_N(t)]$, where each component corresponds to a

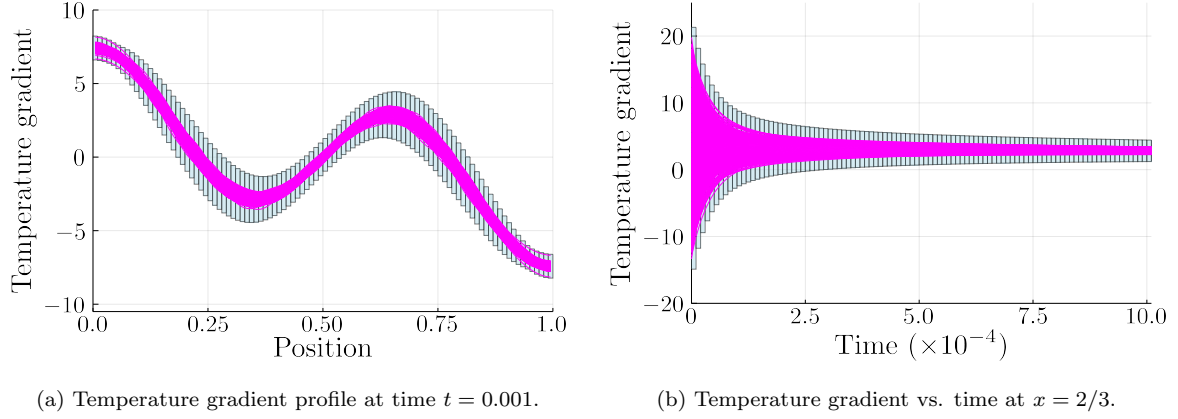


Figure 15: Example 3: Flowpipe (light blue) calculation of the temperature gradient for the same case study from Fig. 14. Superposed are shown several temperature gradients computed with the Backward Euler's method (magenta) with different initial states chosen randomly within the given uncertainty in the initial temperature profile.

different node. We want to compute the differences $T_{i+1}(t) - T_i(t)$ for $i = 1, \dots, N - 1$ (which is then divided by the distance between the two nodes, here considered uniform). Now consider the set of vectors $\{\mathbf{d}_i\}_{1, \dots, N-1}$, where \mathbf{d}_i has length N with all the entries equal to zero, except for the i -th and $(i + 1)$ -th, which are equal to -1 and $+1$ respectively. Then, the scalar product $\langle \mathbf{d}_i, \mathbf{T}(t) \rangle$ gives the temperature difference. This methodology leads to the components of the gradient in the case of higher dimensional problems.

Since it is not clear how to choose the initial temperature profile to obtain an extreme temperature gradient at a given time, here we repeated the calculations with Backward Euler using several different initial temperature profiles (a thousand) chosen randomly from Eq. (53).

The results obtained for the temperature gradient profile at time $t = 0.001$ are shown in Fig. 15a and the time evolution of the temperature gradient at $x = 0.66$ (approximately two thirds of the domain's length) are shown in Fig. 15b. The flowpipe contains all the trajectories calculated with Backward Euler. We remark that statistical strategies are needed to estimate the temperature gradient bounds if we use the last method. On the opposite, the flowpipe gives safe bounds for this gradient with only one integration. We conclude that set propagation is an effective tool to evaluate the maximum temperature under uncertainty.

4.4. Example 4 - concrete casting heat of hydration

In this example a model for heat of hydration during casting of a massive concrete structure is considered. The development of reliable computational models for this kind of processes is a greatly challenging task due to the uncertainty in parameters such as the internal heat generation. In (Wilson et al., 1974), for instance, different levels of heat of hydration (associated with different sizes of aggregate) are considered. The parameter values and the modeling assumptions considered are based on (Bofang, 2014; Tahersima & Tikalsky, 2017).

4.4.1. Problem definition

The domain considered consists in a square cuboid $\Omega = [-1, 1] \times [-1, 1] \times [0, 1]$, with 1 m height (in the z direction) and 2 m width in the other directions (x and y). In Figure 16 the geometry, boundary conditions and control points of the problem are shown.

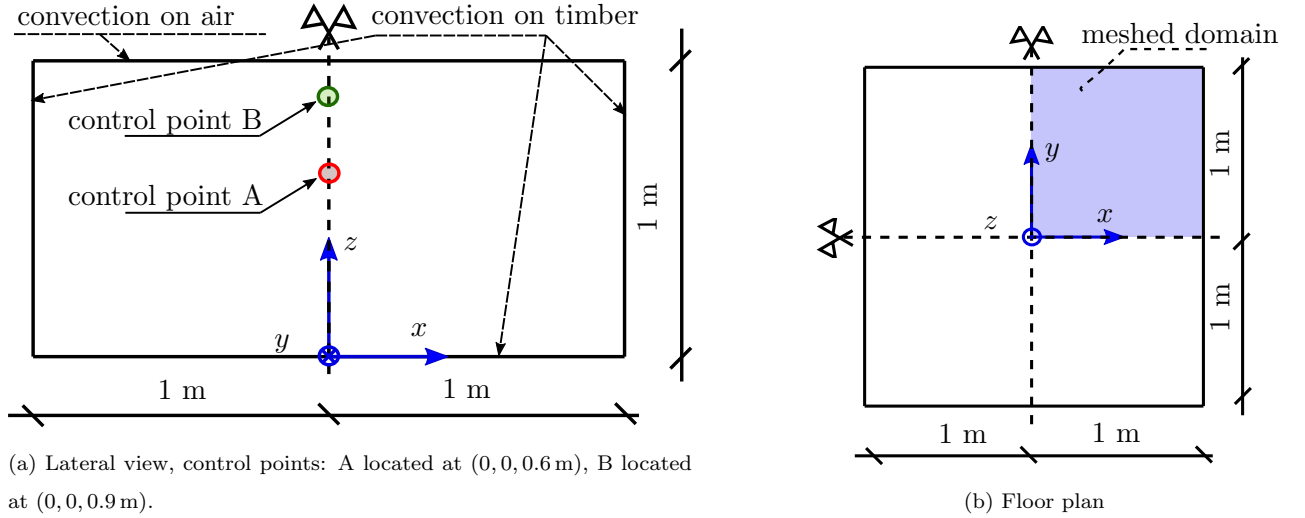


Figure 16: Example 4: diagram of domain, boundary conditions and control points.

The concrete density, the specific heat and the conductivity are considered $\rho = 2485 \text{ kg/m}^3$, $c = 0.967 \text{ kJ/(kg } ^\circ\text{C)}$ and $\kappa = 9.37 \text{ kJ/(m h } ^\circ\text{C)}$, respectively.

Regarding the boundary conditions, on the upper face ($z = 1$) a convection condition is assumed with value $h_{air} = 40 \text{ kJ/(m}^2 \text{ h } ^\circ\text{C)}$, while on the other faces it is $h_{timb} = 500 \text{ kJ/(m}^2 \text{ h } ^\circ\text{C)}$. The external temperature $T_\infty(t)$ dependence in time is assumed to be given by the following sinusoidal law:

$$T_\infty(t) = T_{min} + T_{var} \left(\frac{1}{2} + \frac{1}{2} \sin \left(\omega t - \frac{\pi}{2} \right) \right), \quad (54)$$

where $T_{min} = 17^\circ\text{C}$ is the minimum temperature, T_{var} is the variation or difference between the minimum and maximum temperatures and $\omega = \pi/12 \text{ h}^{-1}$ is the angular frequency. The initial temperature of all the points in the concrete is assumed $T(\mathbf{x}, 0) = T_{min}$, which is equal to the initial external temperature $T_\infty(0)$.

The accumulated heat of hydration is assumed to be given by the exponential law:

$$Q_{AH}(t) = Q_{FH}(1 - e^{-mt}), \quad (55)$$

where Q_{FH} is the final heat of hydration in kJ/kg and $m = 7.95 \times 10^{-3} \text{ h}^{-1}$. This quantity is multiplied by the density, derived and included in the thermal-work Eq. (3) as:

$$Q_{int}(t) = Q_{FH} \cdot \rho \cdot m e^{-mt}. \quad (56)$$

4.4.2. Numerical resolution with fixed parameters

Let us consider the following parameters: $Q_{FH} = 330 \text{ kJ/kg}$ and $T_{var} = 6^\circ\text{C}$. We use a time step $\Delta t = 1/3 \text{ h}$ and the final time of the simulation is 240 hours (10 days). Numerical time integration is done using Backward Euler. The temperature fields obtained at times 0, 10, 50 and 720h are shown in Figure 17. Let us remark that by symmetry, only one quarter of the domain is meshed, and a regular structured mesh of 1331 nodes and 6000 four-node tetrahedron elements is considered.

In order to apply the set propagation method, the source term is factorized using the formulation described in Section 3.1.2. The source term for this model at time t can be written as:

$$\mathbf{f}_\theta(t) = \mathbf{f}_Q Q_{FH} \rho m e^{-mt} + \mathbf{f}_{T_\infty} T_{var} \frac{1}{2} \sin\left(\omega t - \frac{\pi}{2}\right) + \mathbf{f}_{T_\infty} \left(T_{min} + T_{var} \frac{1}{2}\right), \quad (57)$$

where \mathbf{f}_Q and \mathbf{f}_{T_∞} are vectors given by the finite element discretization integration. The terms in Eq. (57) can be factorized to the form of Eq. (36) using:

$$\begin{cases} \mathbf{f}_0^{(1)} = \mathbf{f}_{T_\infty} & \eta^{(1)}(t) = T_{min} + T_{var} \frac{1}{2} \\ \mathbf{f}_0^{(2)} = \mathbf{f}_Q \cdot \rho \cdot m & \eta^{(2)}(t) = Q_{FH} e^{-mt} \\ \mathbf{f}_0^{(3)} = \mathbf{f}_{T_\infty} & \eta^{(3)}(t) = T_{var} \frac{1}{2} \sin\left(\omega t - \frac{\pi}{2}\right). \end{cases} \quad (58)$$

The function $\eta^{(1)}(t)$ can be considered as the solution of the differential equation $\dot{y} = 0$ with initial condition $T_{min} + T_{var} \frac{1}{2}$, the function $\eta^{(2)}$ is the solution of the differential equation $\dot{y} = -my$ with initial condition Q_{FH} and the function $\eta^{(3)}$ is the solution of the differential equation $\ddot{y} + \omega^2 y = 0$ with initial conditions $y(0) = -T_{var} \frac{1}{2}$ and $\dot{y}(0) = 0$.

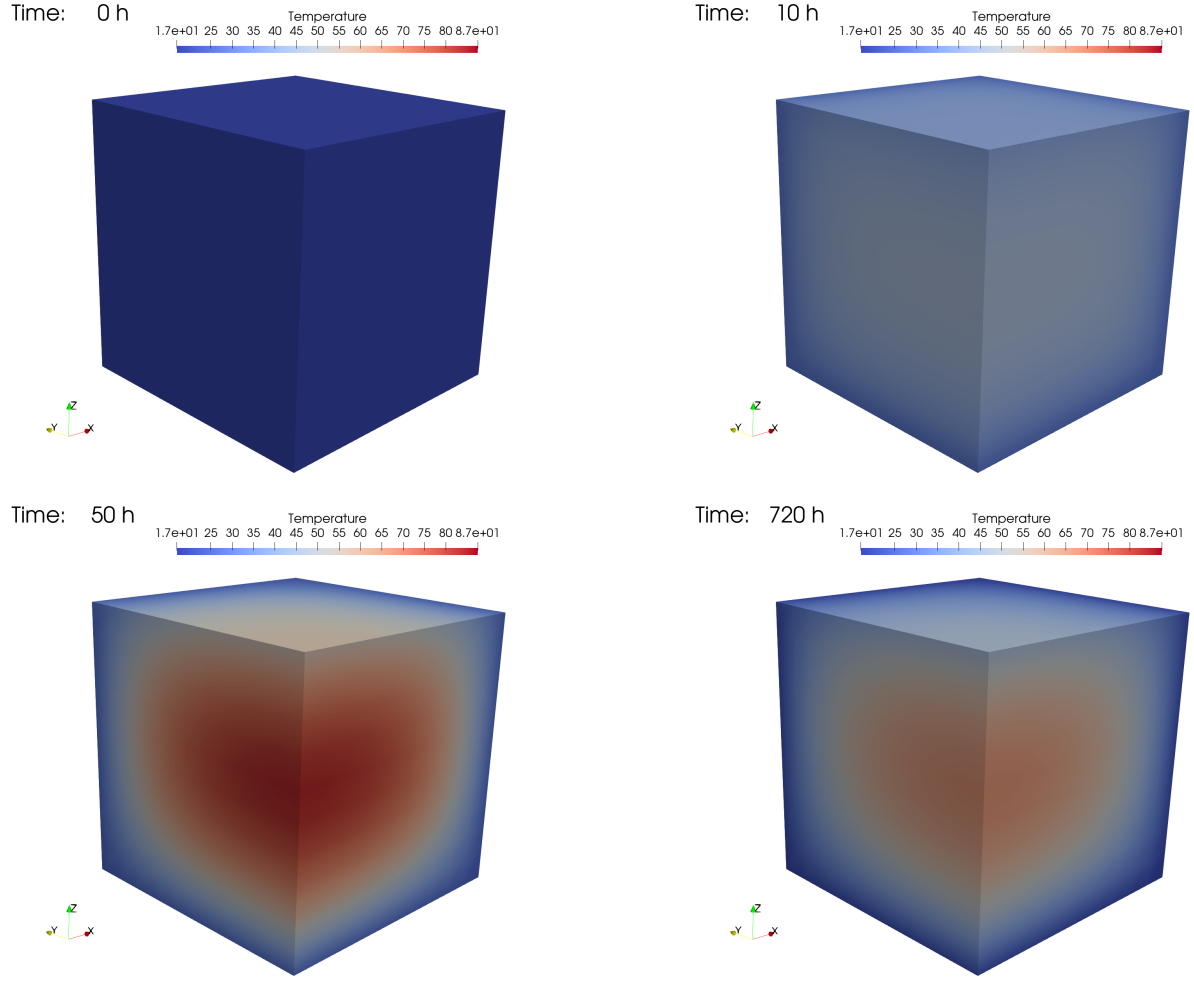


Figure 17: Example 4: Evolution of the temperature field in the meshed domain at four different observation times: 0 h (top-left), 10 h (top-right), 50 h (bottom-left) and 720 h (bottom-right).

This can be written in matrix form as:

$$\begin{bmatrix} \dot{\mathbf{x}} \\ \dot{\xi}_1^{(1)} \\ \dot{\xi}_1^{(2)} \\ \dot{\xi}_1^{(3)} \\ \dot{\xi}_2^{(3)} \end{bmatrix} = \begin{bmatrix} -\mathbf{C}^{-1}\mathbf{K} & -\mathbf{C}^{-1}\mathbf{f}_{T_\infty} & -\mathbf{C}^{-1}\mathbf{f}_{Q\rho m} & -\mathbf{C}^{-1}\mathbf{f}_{T_\infty} & \mathbf{0} \\ \mathbf{0} & 0 & 0 & 0 & 0 \\ \mathbf{0} & 0 & -m & 0 & 0 \\ \mathbf{0} & 0 & 0 & 0 & 1 \\ \mathbf{0} & 0 & 0 & -\omega^2 & 0 \end{bmatrix} \begin{bmatrix} \mathbf{x} \\ \xi_1^{(1)} \\ \xi_1^{(2)} \\ \xi_1^{(3)} \\ \xi_2^{(3)} \end{bmatrix}, \quad (59)$$

Let us solve the problem considering fixed values for the parameters Q_{FH} and T_{var} . In that case, the initial values for the input variables ξ are single fixed values. The evolution of the temperatures obtained in control points A and B is shown in Figure 18.

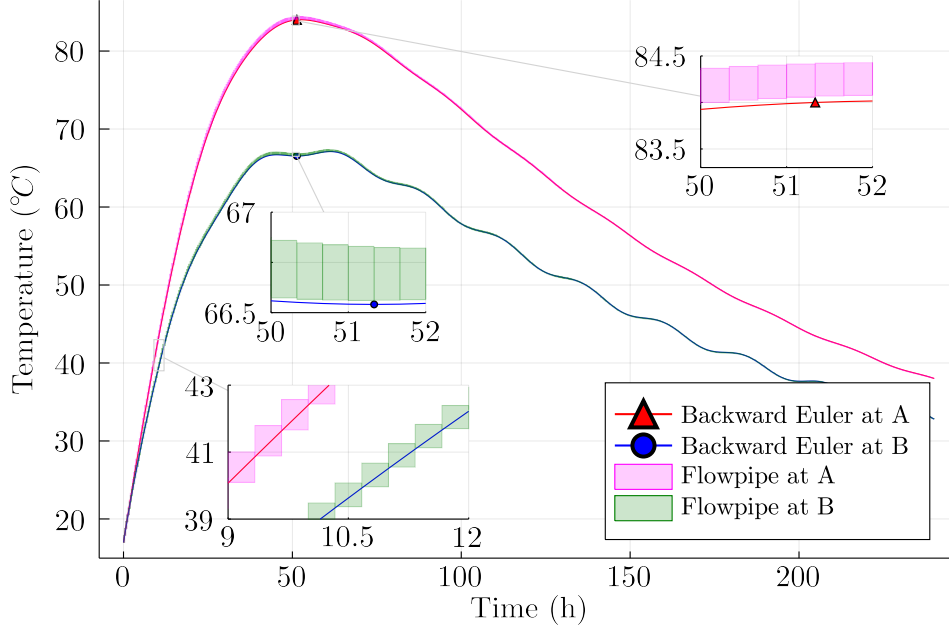


Figure 18: Example 4: temperature evolution at control points A and B.

We observe that the Backward Euler method may underestimate the temperature values, as shown in the zoomed region in Fig. 18 for times within the interval $[50, 52]$ h.

4.4.3. Set propagation under variation in heat sources

Let us consider a variation in the parameters Q_{FH} and T_{var} . For Q_{FH} , a 5% error interval is used, then $Q_{FH} \in [313.5, 346.5]$ kJ/kg, while for T_{amb} , a 2°C variation is considered, then $T_{amb} \in [4, 8]^\circ\text{C}$. These intervals are used to construct the set \mathcal{C}_0 of initial values of the input variables. A plot of the set of accumulated heat functions is shown in Fig. 19.

The flowpipes corresponding to the evolution of the temperature in the control nodes are shown in Fig. 20. The solid lines represent the solution obtained with Backward Euler for the mean values of the parameters (as in Section 4.4.2).

Let us remark that the computational cost of the set-based integration is approximately the same whether we use fixed parameters or parameters with uncertainty. Therefore, reachability analysis becomes an efficient option for safety verification in the design of massive concrete structures under known parameter uncertainty.

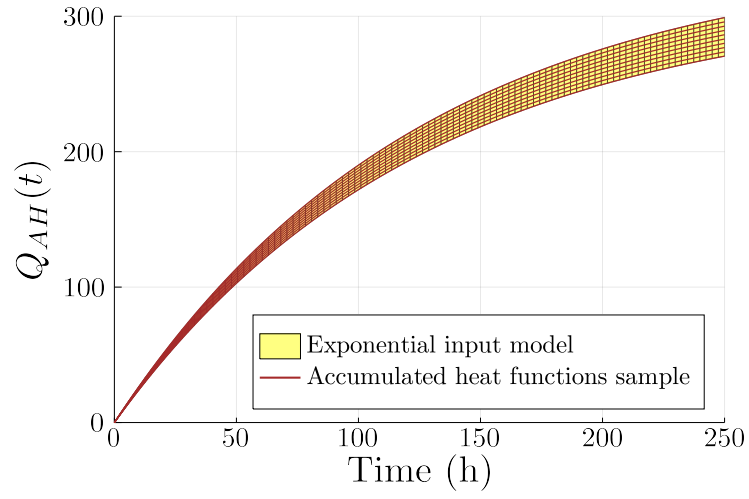


Figure 19: Example 4: plot of the accumulated heat functions considered.

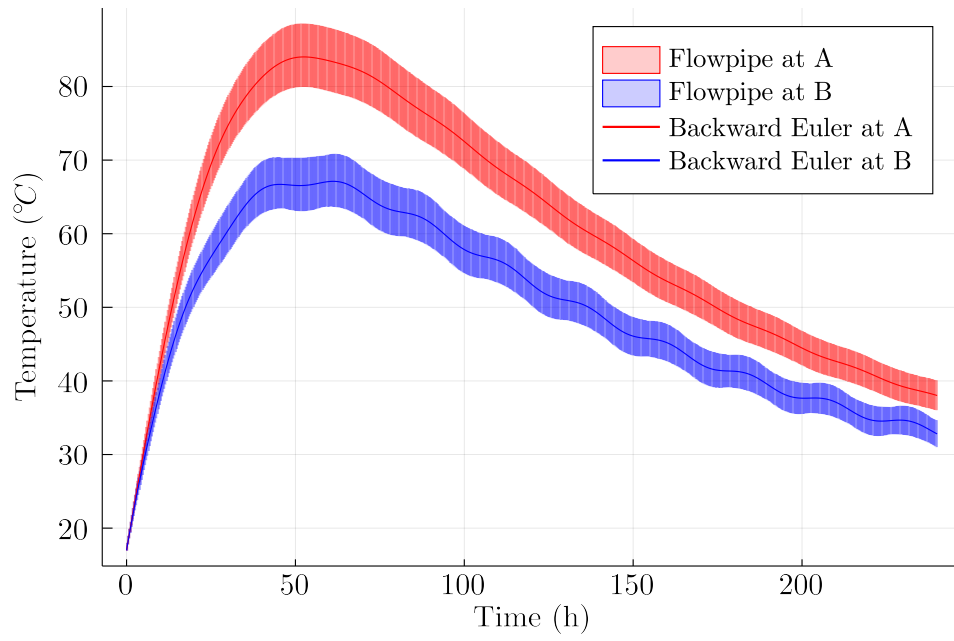


Figure 20: Example 4: results considering variations.

5. Conclusions

In this article a new approach for numerically solving the differential equations that govern linear heat transfer and structural dynamics problems is presented. The approach is based on recent advances in reachability analysis for high-dimensional linear systems. Our work is an attempt to bridge the gap between spatially discretized equations using the Finite Element Method and the incipient field of set-based numerical integration. The results of our approach are compared with reference numerical time integration methods through the resolution of four examples.

The set propagation method consists of computing an initial set that contains all possible trajectories within the time interval $[0, \delta]$, where $\delta > 0$ is the time step of the algorithm, and then propagate that set using set-based techniques. The union of such sets is called the *flowpipe*. Let us remark that, while standard numerical integration provides single values for each time point, our approach returns a *set* for each time interval that is guaranteed to contain all possible solutions of the differential equation for the given initial state(s) and input(s). We found that homogeneization contributes to providing more accurate estimates of the exact flowpipe. We formalized the idea of homogeneization of the governing equations subject to set-based initial conditions and inputs. We also presented a simple modification of an existing theoretical result for conservative time discretization, which ensures more accurate results at a marginal increase in the computational cost. Given that each set representation has its own share of advantages and disadvantages, for each example we analyzed the alternatives and presented the most appropriate approach among the set representations that are most successful in the domain of reachability analysis for linear systems: hyperrectangles, zonotopes and support functions.

In Example 1 a fundamental test problem of a single degree of freedom oscillator, typically used to evaluate numerical properties such as Period Elongation (PE) and Amplitude Decay (AD), was solved. The results obtained let us conclude that the set propagation method has neither PE nor AD. These results represent a remarkable feature in comparison with the Newmark and Bathe methods.

In Example 2 a reference uni-dimensional wave propagation problem is considered. In this example we found that the method can handle a relatively high number of degrees of freedom (two thousand) as well as to accurately integrate a step load function. The solution at a specified node can be efficiently computed using support functions. Moreover, the high-frequency oscillations are

accurately captured by the enclosing flowpipe. We can conclude that for this example, the set propagation method is more accurate than the Newmark and Bathe methods for the same step size.

In Example 3 the set propagation and Backward Euler methods are compared in a unidimensional heat transfer problem. A dense set of spatially distributed initial condition functions is considered. The obtained flowpipe accurately encloses the analytic solution for all initial functions considered. Moreover, we computed the gradient of the solution using a support function approach. To our knowledge, this is the first time that support functions are used to estimate the gradient of a set-based solution. While numerical integration approaches such as Backward Euler require to perform several simulations for different initial functions, the proposed approach provides a robust enclosure with a single set-based integration. Let us remark that computing a high number of simulations to ensure a very high degree of coverage is computationally demanding due to the curse of dimensionality. However, using set propagation the obtained result is robust and requires a single analysis, hence the cost can be drastically reduced.

Finally, the results obtained in Example 4 let us conclude that the set propagation method can be applied to a realistic three-dimensional massive concrete hydration problem. The problem includes a combination of different types of heat sources. The obtained flowpipe is accurate in comparison with numerical solutions, which shows that our homogeneization method can correctly handle various sources of input uncertainty. We observed that for some time intervals the solution obtained using the Backward Euler method underestimates the maximum temperature. Given the theoretical basis of reachability analysis, and the accuracy of our results, we conclude that set propagation may be a useful tool for the design of massive concrete structures.

Several research directions remain open. It would be enlightening to apply the developed method in real engineering problems, in particular in the context of Example 4. For that purpose the theoretical development of other, more general input models might be of interest, as well as the evaluation of the computational cost when the size of the problems increase. The set-based approach might be extended to other scientific domains such as inverse problems and non-linear structural analysis.

Acknowledgements

The authors would like to thank the *Comisión Sectorial de Investigación Científica* of *Universidad de la República* and the *Agencia Nacional de Investigación e Innovación* for the funding of the *Timbó* portal. The authors want also to thank Christian Schilling for valuable discussions at various stages of this work, and Pedro Curto for useful comments in heat transfer analysis.

References

- Ahrens, J., Geveci, B., & Law, C. (2005). Paraview: An end-user tool for large data visualization. *The visualization handbook*, 717.
- Althoff, M. (2019). Reachability analysis of large linear systems with uncertain inputs in the krylov subspace. *IEEE Transactions on Automatic Control*, 65, 477–492.
- Althoff, M., Bak, S., Bao, Z., Forets, M., Frehse, G., Freire, D., Kochdumper, N., Li, Y., Mitra, S., Ray, R. et al. (2020a). ARCH-COMP20 category report: Continuous and hybrid systems with linear continuous dynamics. *EPiC Series in Computing*, 74, 16–48.
- Althoff, M., & Frehse, G. (2016). Combining zonotopes and support functions for efficient reachability analysis of linear systems. In *2016 IEEE 55th Conference on Decision and Control (CDC)* (pp. 7439–7446). IEEE.
- Althoff, M., Frehse, G., & Girard, A. (2020b). Set propagation techniques for reachability analysis. *Annual Review of Control, Robotics, and Autonomous Systems*, 4.
- Althoff, M., Stursberg, O., & Buss, M. (2008). Reachability analysis of nonlinear systems with uncertain parameters using conservative linearization. In *2008 47th IEEE Conference on Decision and Control* (pp. 4042–4048). IEEE.
- Asarin, E., Dang, T., & Girard, A. (2003). Reachability analysis of nonlinear systems using conservative approximation. In *International Workshop on Hybrid Systems: Computation and Control* (pp. 20–35). Springer.
- Bak, S., Tran, H., & Johnson, T. T. (2019). Numerical verification of affine systems with up to a billion dimensions. In *HSCC* (pp. 23–32). ACM.
- Bathe, K.-J. (1982). *Finite Element Procedures in Engineering Analysis*. Prentice-Hall.
- Bathe, K.-J. (2014). *Finite Element Procedures*. (2nd ed.). Watertown, USA.
- Bathe, K.-J., & Noh, G. (2012). Insight into an implicit time integration scheme for structural dynamics. *Computers & Structures*, 98–99, 1–6. URL: <https://linkinghub.elsevier.com/retrieve/pii/S0045794912000107>. doi:10.1016/j.compstruc.2012.01.009.
- Battini, J.-M. (2018). Analysis of dampers for stay cables using non linear beam elements. *Structures*, 16, 45–49. URL: <https://www.sciencedirect.com/science/article/pii/S2352012418300961>. doi:<https://doi.org/10.1016/j.istruc.2018.08.009>.
- Benvenuti, L., Bresolin, D., Casagrande, A., Collins, P., Ferrari, A., Mazzi, E., Sangiovanni-Vincentelli, A., & Villa, T. (2008). Reachability computation for hybrid systems with Ariadne. *IFAC Proceedings Volumes*, 41, 8960–8965.
- Bezanson, J., Edelman, A., Karpinski, S., & Shah, V. B. (2017). Julia: A fresh approach to numerical computing. *SIAM Review*, 59, 65–98.

- Bofang, Z. (2014). *Thermal Stresses and Temperature Control of Mass Concrete*. Elsevier. URL: <https://linkinghub.elsevier.com/retrieve/pii/S0020060383>. doi:10.1016/C2012-0-06038-3.
- Bogomolov, S., Forets, M., Frehse, G., Potomkin, K., & Schilling, C. (2019). JuliaReach: a toolbox for set-based reachability. In *Proceedings of the 22nd ACM International Conference on Hybrid Systems: Computation and Control* (pp. 39–44).
- Bogomolov, S., Forets, M., Frehse, G., Viry, F., Podelski, A., & Schilling, C. (2018). Reach set approximation through decomposition with low-dimensional sets and high-dimensional matrices. In *Proceedings of the 21st International Conference on Hybrid Systems: Computation and Control (part of CPS Week)* (pp. 41–50).
- Brelhoff, T., Schwabeneder, D., Borregaard, M. K., Christ, S., Heinen, J., Yuval, Palugniok, A., Simon, Vertech, P., Zhanibek, Chamberlin, T., ma laforge, Rackauckas, C., Schulz, O., Pfizner, S., Arakaki, T., Yahyaabadi, A., Devine, J., Pech, S., Mogensen, P. K., & Watson, S. S. (2021). JuliaPlots/Plots.jl: v1.13.2. URL: <https://doi.org/10.5281/zenodo.4725318>. doi:10.5281/zenodo.4725318.
- Capillon, R., Desceliers, C., & Soize, C. (2016). Uncertainty quantification in computational linear structural dynamics for viscoelastic composite structures. *Computer Methods in Applied Mechanics and Engineering*, 305, 154–172. URL: <https://www.sciencedirect.com/science/article/pii/S0045782516300949>. doi:<https://doi.org/10.1016/j.cma.2016.03.012>.
- Chen, X., Ábrahám, E., & Sankaranarayanan, S. (2013). Flow*: An analyzer for non-linear hybrid systems. In *International Conference on Computer Aided Verification* (pp. 258–263). Springer.
- Clough, R., & Penzien, J. (1993). *Dynamics of Structures*. McGraw-Hill.
- Eaton, J. W., Bateman, D., Hauberg, S., & Wehbring, R. (2020). *GNU Octave version 5.2.0 manual: a high-level interactive language for numerical computations*. URL: <https://www.gnu.org/software/octave/doc/v5.2.0/>.
- Forets, M., Schilling, C., Caporale, D. F., Benet, L., Sanders, D. P., & Guadalupe, S. (2021). JuliaReach. <https://github.com/JuliaReach/>.
- Frehse, G., Guernic, C. L., Donzé, A., Cotton, S., Ray, R., Lebeltel, O., Ripado, R., Girard, A., Dang, T., & Maler, O. (2011). SpaceEx: Scalable verification of hybrid systems. In *International Conference on Computer Aided Verification* (pp. 379–395). Springer.
- Gérardin, M., & Rixen, D. J. (2014). *Mechanical vibrations: theory and application to structural dynamics*. John Wiley & Sons.
- Geuzaine, C., & Remacle, J.-F. (2009). Gmsh: a three-dimensional finite element mesh generator with built-in pre- and post-processing facilities. *International Journal for Numerical Methods in Engineering*, 79, 1309–1331. doi:10.1002/nme.2579.
- Girard, A., Guernic, C. L., & Maler, O. (2006a). Efficient computation of reachable sets of linear time-invariant systems with inputs. In *HSCC* (pp. 257–271). Springer.
- Girard, A., Le Guernic, C., & Maler, O. (2006b). Efficient computation of reachable sets of linear time-invariant systems with inputs. In *International workshop on hybrid systems: Computation and control* (pp. 257–271). Springer.
- Grau-Bartual, S., & Al-Jumaily, A. M. (2020). Prediction of upper airway dryness and optimal continuous positive airway pressure conditions. *Journal of Biomechanics*, 112, 110037. URL: <https://linkinghub.elsevier.com/>

- retrieve/pii/S0021929020304619. doi:10.1016/j.jbiomech.2020.110037.
- Hecht, F. (2012). New development in freefem++. *Journal of Numerical Mathematics*, 20, 251–265. URL: <http://www.degruyter.com/view/j/jnma.2012.20.issue-3-4/jnum-2012-0013/jnum-2012-0013.xml>. doi:10.1515/jnum-2012-0013.
- Henninger, T. A., Ho, P.-H., & Wong-Toi, H. (1998). Algorithmic analysis of nonlinear hybrid systems. *IEEE transactions on automatic control*, 43, 540–554.
- Hornshøj-Møller, S. D., Nielsen, P. D., Forooghi, P., & Abkar, M. (2021). Quantifying structural uncertainties in Reynolds-averaged Navier–Stokes simulations of wind turbine wakes. *Renewable Energy*, 164, 1550–1558. URL: <https://www.sciencedirect.com/science/article/pii/S0960148120317237>. doi:<https://doi.org/10.1016/j.renene.2020.10.148>.
- Hughes, T. J. R. (1987). *The Finite Element Method*. (1st ed.). Prentice-Hall.
- Imholz, M., Faes, M., Vandepitte, D., & Moens, D. (2020). Robust uncertainty quantification in structural dynamics under scarce experimental modal data: A bayesian-interval approach. *Journal of Sound and Vibration*, 467, 114983. URL: <https://www.sciencedirect.com/science/article/pii/S0022460X19305450>. doi:<https://doi.org/10.1016/j.jsv.2019.114983>.
- Kim, W., & Choi, S. Y. (2018). An improved implicit time integration algorithm: The generalized composite time integration algorithm. *Computers & Structures*, 196, 341–354. URL: <https://linkinghub.elsevier.com/retrieve/pii/S0045794917303413>. doi:10.1016/j.compstruc.2017.10.002.
- Ladeveze, P., & Leguillon, D. (1983). Error Estimate Procedure in the Finite Element Method and Applications. *SIAM Journal on Numerical Analysis*, 20, 485–509. URL: <http://epubs.siam.org/doi/abs/10.1137/0720033>. doi:10.1137/0720033.
- Le Guernic, C. (2009). *Reachability analysis of hybrid systems with linear continuous dynamics*. Ph.D. thesis Université Grenoble 1 - Joseph Fourier.
- Le Guernic, C. (2009). Reachability analysis of hybrid systems with linear continuous dynamics. *Ph.D. dissertation, Université Joseph-Fourier-Grenoble I*, .
- Le Guernic, C., & Girard, A. (2010). Reachability analysis of linear systems using support functions. *Nonlinear Analysis: Hybrid Systems*, 4, 250–262.
- Le Guernic, C., & Girard, A. (2010). Reachability analysis of linear systems using support functions. *Nonlinear Analysis: Hybrid Systems*, 4, 250 – 262. IFAC World Congress 2008.
- Li, E., He, Z., Tang, Q., & Zhang, G. (2017). Large time steps in the explicit formulation of transient heat transfer. *International Journal of Heat and Mass Transfer*, 108, 2040–2052. URL: <https://linkinghub.elsevier.com/retrieve/pii/S0017931016324607>. doi:10.1016/j.ijheatmasstransfer.2017.01.065.
- Maas, S. A., Ellis, B. J., Ateshian, G. A., & Weiss, J. A. (2012). FEBio: Finite Elements for Biomechanics. *Journal of Biomechanical Engineering*, 134. URL: <https://asmedigitalcollection.asme.org/biomechanical/article/doi/10.1115/1.4005694/455684/FEBio-Finite-Elements-for-Biomechanics>. doi:10.1115/1.4005694.
- Malakiyeh, M. M., Shojaee, S., & Bathe, K.-J. (2019). The Bathe time integration method revisited for prescribing desired numerical dissipation. *Computers & Structures*, 212, 289–298. URL: <https://linkinghub.elsevier.com/retrieve/pii/S0045794918310046>. doi:10.1016/j.compstruc.2018.10.008.

- Martinelli, L., & Perotti, F. (2001). Numerical analysis of the non-linear dynamic behaviour of suspended cables under turbulent wind excitation. *International Journal of Structural Stability and Dynamics*, 1, 207–233.
- Muhanna, R. L., & Mullen, R. L. (1999). Formulation of fuzzy finite-element methods for solid mechanics problems. *Computer-Aided Civil and Infrastructure Engineering*, 14, 107–117.
- Muhanna, R. L., & Mullen, R. L. (2011). Interval based finite elements for uncertainty quantification in engineering mechanics. In *IFIP Working Conference on Uncertainty Quantification* (pp. 265–279). Springer.
- Oñate, E. (2009). *Structural Analysis with the Finite Element Method* volume 1 of *Lecture Notes on Numerical Methods in Engineering and Sciences*. Dordrecht: Springer Netherlands. URL: <http://link.springer.com/10.1007/978-1-4020-8733-2>. doi:10.1007/978-1-4020-8733-2.
- Patiño, S., Pérez Zepa, J., & Fariña, R. (2019). Finite element and morphological analysis in extant mammals’ claws and quaternary sloths’ ungual phalanges. *Historical Biology*, . doi:10.1080/08912963.2019.1664504.
- Prajapat, G. P., Senroy, N., & Kar, I. N. (2017). Wind Turbine Structural Modeling Consideration for Dynamic Studies of DFIG Based System. *IEEE Transactions on Sustainable Energy*, 8, 1463–1472. URL: <http://ieeexplore.ieee.org/document/7892018/>. doi:10.1109/TSTE.2017.2690682.
- Pérez Zepa, J. M., Bazzano, J. B., Viera, J., Vanzulli, M., Forets, M., Battini, J.-M., & Toro, S. (2021). Open nonlinear structural analysis solver ONSAS. <https://github.com/ONSAS/ONSAS.m/>.
- Romano, G., Diaco, M., & Barretta, R. (2010). Variational Formulation of the First Principle of Continuum Thermodynamics. *Continuum Mechanics and Thermodynamics*, 22, 177–187. URL: <http://link.springer.com/10.1007/s00161-009-0119-z>. doi:10.1007/s00161-009-0119-z.
- Scacchioli, A., Bayen, A. M., & Stojadinović, B. (2014). Assessment of uncertainty propagation in the dynamic response of single-degree-of-freedom structures using reachability analysis. *Journal of Engineering Mechanics*, 140, 04014038.
- Shinozuka, M. (1972). Monte carlo solution of structural dynamics. *Computers & Structures*, 2, 855–874.
- Shu-Xiang, G., & Zhen-zhou, L. (2001). Interval arithmetic and static interval finite element method. *Applied Mathematics and Mechanics*, 22, 1390–1396.
- Tahersima, M., & Tikalsky, P. (2017). Finite element modeling of hydration heat in a concrete slab-on-grade floor with limestone blended cement. *Construction and Building Materials*, 154, 44–50. URL: <https://linkinghub.elsevier.com/retrieve/pii/S0950061817315180>. doi:10.1016/j.conbuildmat.2017.07.176.
- Urquiza, S., Blanco, P., Vénere, M., & Feijóo, R. (2006). Multidimensional modelling for the carotid artery blood flow. *Computer Methods in Applied Mechanics and Engineering*, 195, 4002–4017. URL: <https://linkinghub.elsevier.com/retrieve/pii/S0045782505003440>. doi:10.1016/j.cma.2005.07.014.
- Wetzlinger, M., Kochdumper, N., & Althoff, M. (2020). Adaptive parameter tuning for reachability analysis of linear systems. In *2020 59th IEEE Conference on Decision and Control (CDC)* (pp. 5145–5152). IEEE.
- Wilson, E., Bathe, K., & Peterson, F. (1974). Finite element analysis of linear and nonlinear heat transfer. *Nuclear Engineering and Design*, 29, 110–124. URL: <https://linkinghub.elsevier.com/retrieve/pii/0029549374901010>. doi:10.1016/0029-5493(74)90101-0.
- Xue, Z., Wang, W., Fang, L., & Zhou, J. (2020). Numerical simulation on structural dynamics of 5 MW wind turbine. *Renewable Energy*, 162, 222–233. URL: <https://linkinghub.elsevier.com/retrieve/pii/S0960148120312659>.

doi:10.1016/j.renene.2020.08.028.

Zienkiewicz, O. C. (1972). *Introductory Lectures on the Finite Element Method*. Vienna: Springer Vienna. URL: <http://link.springer.com/10.1007/978-3-7091-2973-9>. doi:10.1007/978-3-7091-2973-9.

Appendix A. Proof of Proposition 1

Using the forward-only transformations in (Bogomolov et al., 2018) applied to the special case when the system is homogeneous,

$$\Omega_0^+ = CH(\mathcal{X}_0, \Phi \mathcal{X}_0 \oplus E^+(\mathbf{A}, \mathcal{X}_0, \delta)), \quad (\text{A.1})$$

where $E^+(\mathbf{A}, \mathcal{X}_0, \delta) = \square(\mathbf{P}(|\mathbf{A}|, \delta) \square (\mathbf{A}^2 \mathcal{X}_0))$ and $\mathbf{P}(\mathbf{A}, \delta) = \sum_{i=0}^{\infty} \mathbf{A}^i \delta^{i+2} / (i+2)!$, $\delta > 0$.

The exact reachable set at the time point $t = \delta$ is $\mathcal{R}^e(\mathcal{X}_0, \delta) = \Phi \mathcal{X}_0$. Under the transformation $t \mapsto -t$, the state transition matrix of the linear system (26) becomes $\Phi^{-1} = e^{-\mathbf{A}\delta}$. Therefore the reachable states for the time interval $[0, \delta]$ can be enclosed using Eq. (A.1) backwards in time:

$$\begin{aligned} \Omega_0^- &= CH(\Phi \mathcal{X}_0, \Phi^{-1} \Phi \mathcal{X}_0 \oplus E^+(-\mathbf{A}, \Phi \mathcal{X}_0, \delta)) \\ &= CH(\Phi \mathcal{X}_0, \mathcal{X}_0 \oplus E^+(\mathbf{A}, \Phi \mathcal{X}_0, \delta)). \end{aligned} \quad (\text{A.2})$$

Since both Ω_0^+ and Ω_0^- are sound overapproximations of $\mathcal{R}^e(\mathcal{X}_0, [0, \delta])$, we conclude that

$$\mathcal{R}^e(\mathcal{X}_0, [0, \delta]) \subseteq \Omega_0^+ \cap \Omega_0^-. \quad (\text{A.3})$$

The convergence property follows from Lemma 3 in (Frehse et al., 2011).

Appendix B. Proof of Proposition 2

Let $H_0 = \langle \mathbf{c}_0, \mathbf{r}_0 \rangle_H$ be the initial hyperrectangle. It can be represented as a zonotope with a diagonal generators matrix, $Z_0 = \langle \mathbf{c}_0, \mathbf{D}_0 \rangle_Z$ where \mathbf{D}_0 is the diagonal matrix whose entries are the elements of \mathbf{r}_0 . Using Eq. (46), let $Z_k = \langle \mathbf{c}_k, \mathbf{G}_k \rangle_Z$ such that $\mathbf{c}_k = \Phi^k \mathbf{c}_0$ and $\mathbf{G}_k = \Phi^k \mathbf{D}_0$ for each $k \geq 0$. From Prop. 2.2 in Le Guernic (2009), the support function of $Z = \langle \mathbf{c}, \mathbf{G} \rangle_Z$ along direction $\mathbf{d} \in \mathbb{R}^n$ is

$$\rho(\mathbf{d}, Z) = \mathbf{d}^T \mathbf{c} + \|\mathbf{G}^T \mathbf{d}\|_1 = \sum_{i=1}^n d_i c_i + \sum_{i=1}^n \left| \sum_{j=1}^n (\mathbf{G})_{ji} d_j \right|. \quad (\text{B.1})$$

Let $\mathbf{d} = \pm \mathbf{e}_i$ for any $i = 1, \dots, n$ be a canonical direction (and its opposite). Then,

$$\begin{aligned} \rho(\pm \mathbf{e}_i, Z_k) &= (\pm \mathbf{c}_k)_i + \sum_{i'=1}^n |(\mathbf{G}_k)_{ii'}| = (\pm \Phi^k \mathbf{c}_0)_i + \sum_{i'=1}^n |(\Phi^k \mathbf{D}_0)_{ii'}| \\ &= (\pm \Phi^k \mathbf{c}_0)_i + \left(|\Phi^k| \mathbf{r}_0 \right)_i. \end{aligned} \quad (\text{B.2})$$

Therefore, the radius of the tight hyperrectangular overapproximation of Z_k , $H_k = \langle \mathbf{c}_k, \mathbf{r}_k \rangle_H$, along direction \mathbf{e}_i is

$$(\mathbf{r}_k)_i = \frac{\rho(\mathbf{e}_i, Z_k) + \rho(-\mathbf{e}_i, Z_k)}{2} = \left(|\Phi^k| \mathbf{r}_0 \right)_i, \quad (\text{B.3})$$

which concludes the proof.

Appendix C. Estimation of PE and AD in Flowpipes

In this section we describe a numerical procedure for the computation of Period Elongation (PE) and Amplitude Decay (AD) for the set propagation method results presented in Example 1.

This problem can be reduced to the computation of T_{num} for Eq. (48) and A_{num} for Eq. (49). In order to compute amplitudes and periods, maximums of the flowpipe solution have to be identified.

Let us consider a flowpipe \mathcal{F} formed by the union of a finite number of reach-sets $\{X_k\}_k$. The relative maximum of the displacement happens when the conditions $u(t) > 0$ and $v(t) = 0$ are met. The intersection of \mathcal{F} with the set $U^+ = \{(u, v) \in \mathbb{R}^2 : (u > 0) \wedge (v = 0)\}$ results in one or several reach-sets such that their intersection with U^+ is non-empty, i.e. they include the behavior that satisfies the maximum displacement conditions (if more than one reach-set intersects U^+ , we take their set union).

To estimate a period T_{num} to the flowpipe \mathcal{F} we proceed as follows. Let \mathcal{T}_m be the time interval associated with the m -th intersection of \mathcal{F} with U^+ . Then, we have $m \cdot T_{num} \in \mathcal{T}_m$ for any period m , therefore we can define the following time interval:

$$S_T = \bigcap_m \mathcal{T}_m \frac{1}{m}. \quad (\text{C.1})$$

Since S_T is an intersection of intervals, all containing T_{num} , then

$$T_{num} \in S_T. \quad (\text{C.2})$$

We repeated the same example for different values of α and calculated S_T in each case using 1000 periods. The value of PE reported in Fig. 8a corresponds to the maximum of T_{num} among all periods.

Regarding the estimation of the amplitude, using the time intersection in Eq. (C.1) we compute an interval of displacements. The lower value of displacement represents a safe estimation of the amplitude, and also the worst possible case for the Amplitude Decay. This is the value considered for the computation of AD in Fig. 8b.